The Formation of Parasitic Capillary Ripples on Gravity–Capillary Waves and the Underlying Vortical Structures

LI-PING HUNG AND WU-TING TSAI

Institute of Hydrological and Oceanic Sciences, National Central University, Taoyuan, Taiwan

(Manuscript received 29 January 2008, in final form 20 August 2008)

ABSTRACT

The evolution of moderately short, steep two-dimensional gravity–capillary waves, from the onset of the parasitic capillary ripples to a fully developed quasi-steady stage, is studied numerically using a spectrally accurate model. The study focuses on understanding the precise mechanism of capillary generation, and on characterizing surface roughness and the underlying vortical structure associated with parasitic capillary waves. It is found that initiation of the first capillary ripple is triggered by the fore–aft asymmetry of the otherwise symmetric carrier wave, which then forms a localized pressure disturbance on the forward face near the crest, and subsequently develops an oscillatory train of capillary waves. Systematic numerical experiments reveal that there exists a minimum crest curvature of the carrier gravity–capillary wave for the formation of parasitic capillary ripples, and such a threshold curvature ($\approx$0.25 cm^{-1}) is almost independent of the carrier wavelength. The characteristics of the parasitic capillary wave train and the induced underlying vortical structures exhibit a strong dependence on the carrier wavelength. For a steep gravity–capillary wave with a shorter wavelength (e.g., 5 cm), the parasitic capillary wave train is distributed over the entire carrier wave surface at the stage when capillary ripples are fully developed. Immediately underneath the capillary wave train, weak vortices are observed to confine within a thin layer beneath the ripple crests whereas strong vortical layers with opposite orientation of vorticity are shed from the ripple troughs. These strong vortical layers are then convected upstream and accumulate within the carrier wave crest, forming a strong "capillary roller" as postulated by Longuet-Higgins. In contrast, as the wavelength of the gravity–capillary wave increases (e.g., 10 cm), parasitic capillary ripples appear as being trapped in the forward slope of the carrier wave. The strength of the vortical layer shed underneath the parasitic capillaries weakens, and its thickness and extent reduces. The vortices accumulating within the crest of the carrier wave, therefore, are not as pronounced as those observed in the shorter gravity–capillary waves.

1. Introduction

Capillary ripples riding on longer gravity-dominant carrier waves are commonly observed on ocean surfaces. These parasitic capillary waves, with length scales ranging from a few centimeters down to fractions of millimeters, can be distributed over the entire surface or trapped on the leading slope of carrier waves. The formation of parasitic capillary waves is of fundamental importance in remote sensing of ocean surfaces involving microwave scattering by surface roughness (e.g., Gade et al. 1998; Plant 1997). Their presence can also change the flow processes within the sublayer immediately beneath the ocean surface, and accordingly, significantly influence the transport of gas and heat across the air–water interface (e.g., Peirson and Banner 2003).

Cox (1958), in a pioneering laboratory study, pointed out the occurrence of high-frequency waves trapped on the forward face of a wind-generated gravity wave. As the wind speed increases, ripples are also observed on the rear face together with a persistent leading face trapping of ripples. Cox's measurements also indicate the importance of nonlinear effects associated with these high-frequency ripples on dominant gravity waves. Analysis explaining the generation of parasitic capillary ripples on a gravity–capillary wave (GCW) was first given by Longuet-Higgins (1963). The generation mechanism is attributed to localized normal stresses arising from surface tension effects near the sharp GCW crest; capillary waves can be generated without the action of wind. Subsequent laboratory experiments (e.g., Chang

Corresponding author address: Wu-Ting Tsai, Institute of Hydrological and Oceanic Sciences, National Central University, Taoyuan 32001, Taiwan.
E-mail: wttsai@ncu.edu.tw

DOI: 10.1175/2008JPO3992.1

et al. 1978; Ermakov et al. 1986; Ebuchi et al. 1987; Perlin et al. 1993; Zhang 1995; Fedorov et al. 1998) and theoretical analyses (e.g., Ruvinsky et al. 1991; Longuet-Higgins 1995; Watson and Buchsbaum 1996; Fedorov and Melville 1998) confirmed the existence of parasitic capillary ripples and indicated their generation mechanism on a GCW.

The first attempt to understand the flow structures underneath a wind-generated GCW was made by Okuda (1982). His laboratory experiment by flow visualization identified a region of high vorticity, or a roller, underneath the crest of the carrier wave. [Such a feature was also pointed out by Ebuchi et al. (1987), who conducted the experiment in the same wind–wave flume as that of Okuda (1982), but focused on studying the surface structures on wind–wave surfaces.] Okuda attributed the occurrence of such a high-vorticity region to large local tangential wind stress on the windward face near the crest of the carrier wave. Longuet-Higgins (1992) proposed another explanation, and argued that a very likely source of the crest vorticity is the parasitic capillaries close to the forward edge of the vorticity region; the crest roller and the capillaries form a cooperative system, each sustaining the other. He also suggested that the direct effect of the wind in producing a crest roller is small compared to that of the capillaries.

Later numerical simulations and laboratory experiments, nevertheless, reveal a different picture of the vorticity distribution from that observed in the experiments of Okuda (1982), and argued theoretically by Longuet-Higgins (1992). Mui and Dommermuth (1995) conducted the first Navier–Stokes simulation of a fully nonlinear, free-propagating GCW to study the underlying boundary layer and the associated vortical structure. The strong vortical region in the crest of the GCW is absent in their numerical simulations; instead, they identified a weak crest vortex with a sign opposite to that observed by Okuda (1982) and argued by Longuet-Higgins (1992). They conjectured that a strong crest roller with a sign that corresponds to the results of Okuda (1982), Ebuchi et al. (1987), and Longuet-Higgins (1992) could only form under the action of wind; the mere diffusion of the vorticity from underneath the parasitic capillaries is not sufficient to generate a crest roller. Such a result seems to be supported by a more recent laboratory experiment by Lin and Perlin (2001), who have applied the particle–imaging–velocimetry technique to measure the near-surface velocity fields beneath free-propagating GCWs with parasitic ripples. Lin and Perlin (2001) did not observe strong vorticity regions underneath the GCW crests for the three GCW wavelengths (5, 7, and 10 cm) they considered; this is in agreement with the simulation result of Mui and Dommermuth (1995).

The above contrary findings concerning vortical structures underneath GCWs with parasitic capillary ripples motivated the present study. By using a recently developed, spectrally accurate numerical model (Tsai and Hung 2007), the evolution of moderately short, steep GCWs from the onset of the parasitic capillaries to a fully developed quasi-steady stage, is studied numerically The objectives of the present numerical simulations are twofold: 1) to reappraise the precise mechanism of the generation of parasitic capillaries and the subsequent evolution of the GCW and 2) to clarify the contrary vortical structures underneath the GCW crest reported in the previous studies by revealing the source and transport of the vorticity field. The variability and the characteristics of the parasitic capillary waves are also explored by conducting simulations with various wavelengths and steepnesses of the GCWs.

The paper is organized as follows. The numerical model and the implementation of the simulation are first summarized in section 2. The evolution of the surface waves is then reported in section 3. The characteristics of the parasitic capillary wave train are discussed in section 4 by showing various properties deduced from the simulations and by comparing the present numerical results with previous experimental measurements. The underlying flow structures associated with the parasitic capillary ripples are presented in section 5. The process of vortex shedding by the presence of capillary ripples and its transport as a contributing factor in the formation of the crest roller are discussed in section 6. The paper concludes with discussions on the impact of wind stress on the formation of parasitic capillary waves, and on the explanation of the contrary vortical structures observed by Mui and Dommermuth (1995) and Lin and Perlin (2001), and postulated by Longuet-Higgins (1992). (Supplemental material is available online at the Journals Online Web site http://dx.doi.org/10.1175/2009JPO3992.sl.)

2. Numerical model and simulation implementation

We consider the two-dimensional flow of a viscous fluid bounded by a free-moving water surface: $z = \eta(x,t)$. The surface–tension effect (with a constant surface tension $\sigma = 0.073\ \mathrm{N\ m^{-1}}$) is incorporated for the present study of GCW. The fluid, with a density $\rho = 1000\ \mathrm{kg\ m^{-3}}$ and a kinematic viscosity $\nu = 10^{-6}\ \mathrm{m^2\ s^{-1}}$, is assumed to be incompressible and Newtonian such that the velocity (u,w) and the dynamic pressure p are governed by the solenoidal condition and the Navier–Stokes equations. Cyclic conditions are employed in the horizontal directions; and a free-slip condition is imposed on the lower boundary. Balance of the tangential and normal stresses, respectively, on the free-surface boundary results in tangential-stress and normal-stress dynamic conditions. The free-surface boundary is a material surface that gives rise to a kinematic condition governing the deformation and motion of the wavy surface.

A numerical model has been developed for simulating such a fully nonlinear free-surface flow by the present authors. Details of the model formulation and numerics, and the model capabilities for resolving surface waves of various length scales, ranging from the gravity waves to capillary ripples, are reported in Tsai and Hung (2007). With the focus being on understanding the detailed process of parasitic-capillary generation and the associated underlying vortical structure, only the two-dimensional version of the three-dimensional model is adopted in the present study.

The simulation is started with a nonlinear progressive gravity wave of wavelength λ and steepness a_0k, where a_0 is half that of the initial wave height $H_0 = 2a_0$ and $k = 2\pi/\lambda$ is the wavenumber. The initial surface elevation and the velocity field are specified by the steady Stokes–wave solution of Fenton (1988). Accordingly, the GCW is initiated with an irrotational flow field without any prescribed capillary ripples and vortical structures. Noted that such an assumption to initiate the GCW simulation with a pure gravity wave may become unrealistic for very short GCWs with large amplitude. It has been demonstrated both theoretically (Chen and Saffman 1979; Hogan 1980) and numerically (Chen and Saffman 1980; Schwartz and Vanden-Broeck 1979) that in this range of parameters, several classes of solutions would exist for a steady, symmetric, progressive GCW. In particular the analysis of Chen and Saffman (1979) showed the existence of continuous bifurcation between waves of degree 1 and (1,N) due to resonant interactions between the fundamental and the Nth harmonic and leading to the formation of ($N - 1$) capillaries along the profile of the basic wave. These results indicate the complexity of the combined gravity–capillary wave even in the case of steady, symmetric wave. The focuses of the present numerical experiment are on the formation process of capillary ripples ridding on the dominant gravity wave and the associated rotational flow structures underneath. The use of a pure gravity wave as the initial condition, therefore, is aimed to trigger the initial capillary ripples and to isolate the generation mechanism. It can be shown numerically that for the posed initial condition the computed transient wave converges to a unique solution as the number of grids increases (see below). It is possible that variation in the initial condition may lead to different classes of transient solutions due to nonlinear resonant interactions as revealed by Chen and Saffman (1979) for the steady,

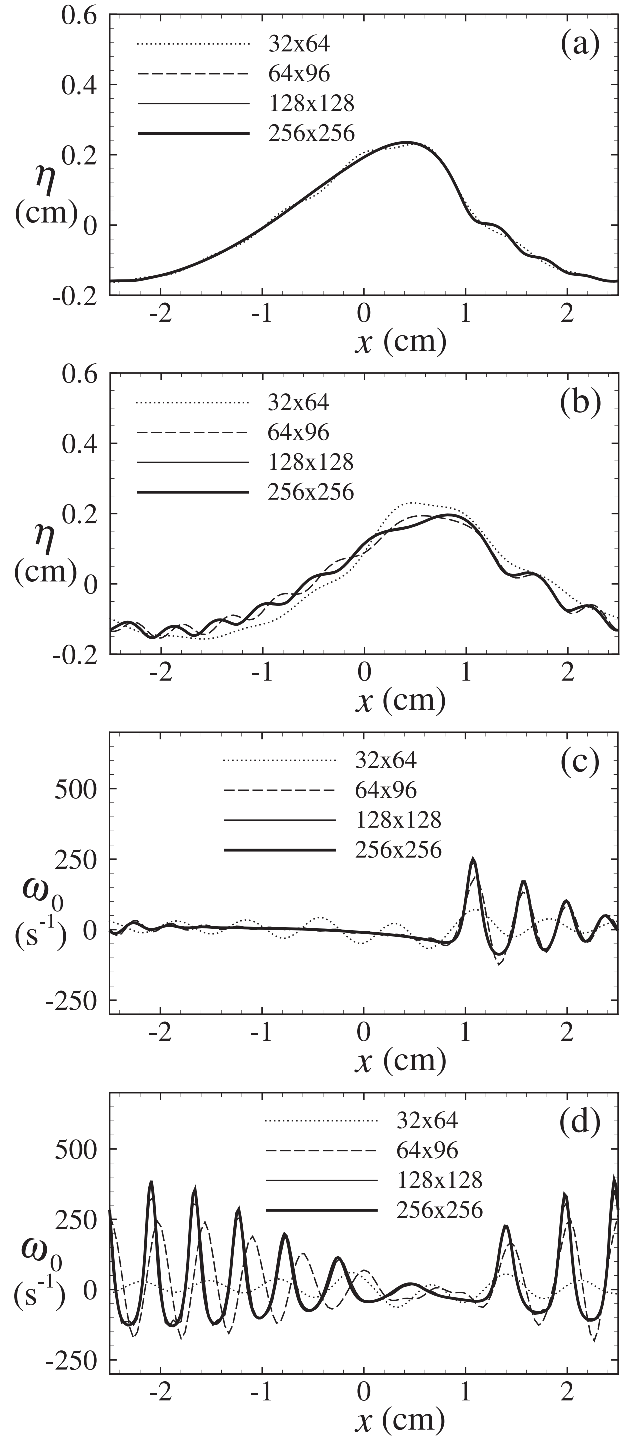

FIG. 1. Computation results of (a),(b) surface elevation η and (c),(d) vorticity ω_0 using grid resolutions (horizontal grids $\times$ vertical grids): 32×64 (dotted lines), 64×96 (dashed lines), 128×128 (solid lines), and 256×256 (thick solid lines) for the GCW with wavelength $\lambda = 5$ cm and initial steepness $a_0k = 0.25$ at two representative times (a),(c) $t = T_0$ and (b),(d) $3T_0$. The GCW propagates from left to right.

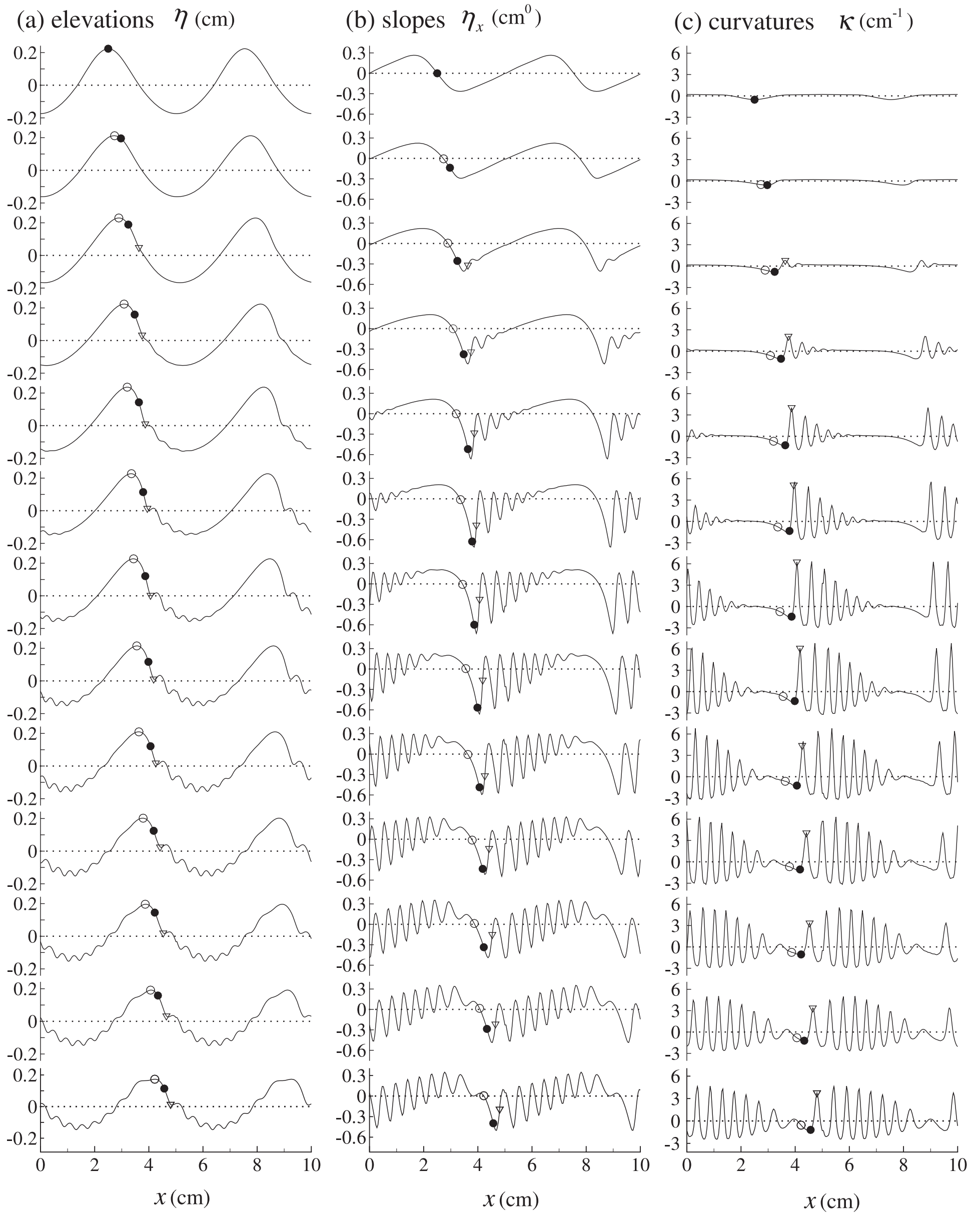

FIG. 2. Evolution of the (a) surface elevation η, (b) the surface slope η_x, and (c) the surface curvature κ of the GCW with wavelength $\lambda = 5$ cm and initial steepness $a_0k = 0.25$. The GCW, which is periodic in space, propagates from left to right. For clarity, the periodic domain is repeated twice and the frame of reference moves with the linear phase speed c_0. (top to the bottom) The instantaneous profiles are at the time intervals $t = nT_0/4$, where n is integer ranging from 0 to 12. The instantaneous locations of the maximum elevation of the crest, the local maximum convex curvature, and the local maximum concave curvature are marked with an open circle, a solid circle, and an open triangle, respectively. The GCW propagates from left to right.

symmetric GCW. This will be a matter for further study.

To compare with the previous experimental measurements (Okuda 1982; Ermakov et al. 1986; Fedorov et al. 1998; Lin and Perlin 2001) and numerical simulation of Mui and Dommermuth (1995), the simulations are conducted for four GCW wavelengths (3.9, 5, 7, and 10 cm) with various GCW steepnesses. As will be discussed in the later sections, the characteristics of the parasitic capillaries and the underlying velocity field vary drastically for the range of GCW wavelengths considered. As such, the required grid resolution to achieve a

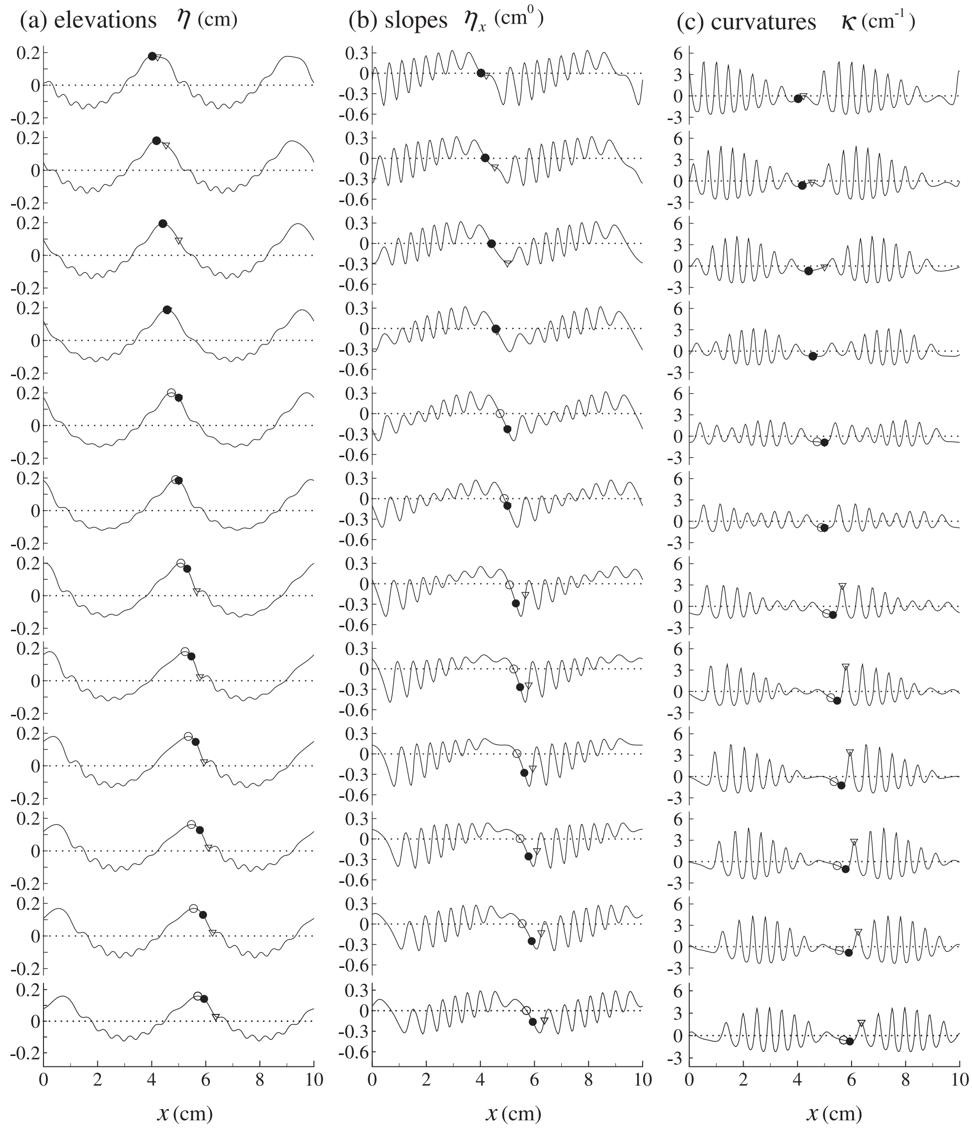

FIG. 3. Consecutive evolution of surface profiles following that of Fig. 2. (top to the bottom) The instantaneous profiles are at the time intervals $t = nT_0/4$, where n is integer ranging from 13 to 24.

converged numerical solution of the simulation also depends on the GCW wavelength. To assure the convergence and accuracy of the simulation, we increase the number of the computational grids until the computed surface elevation and velocity field do not change with the grid resolution.

To demonstrate the convergence property of the computations, distributions of surface elevation η and vorticity ω_0 using various grid resolutions are depicted in Fig. 1 for GCW of $\lambda = 5$ cm with an initial steepness $a_0k = 0.25$. Note that vorticity is related to velocity gradients. As shown in Figs. 1a,b, the computed surface elevations are virtually indistinguishable for the simulations using 128^2 and 256^2 grid resolutions. Very small deviations are observed at some local maximum of the surface vorticity distribution at some later time of the simulation (Fig. 1d). The result indicates that a 128^2 grid resolution will be sufficient for the simulations of $\lambda = 5$ cm. Similar systematic numerical experiments conclude that for the computations of $\lambda = 3.9$ and 7 cm, a resolution with 128 grids in both horizontal and vertical directions will result in converged solutions. For the case of $\lambda = 10$ cm, a much finer resolution with 384 grids in both horizontal and vertical directions is needed.

For temporal integration of the velocity field and the surface elevation, discrete time steps $T_0/2000$ and $T_0/4000$ are used for the 128^2 and 384^2 grid resolution

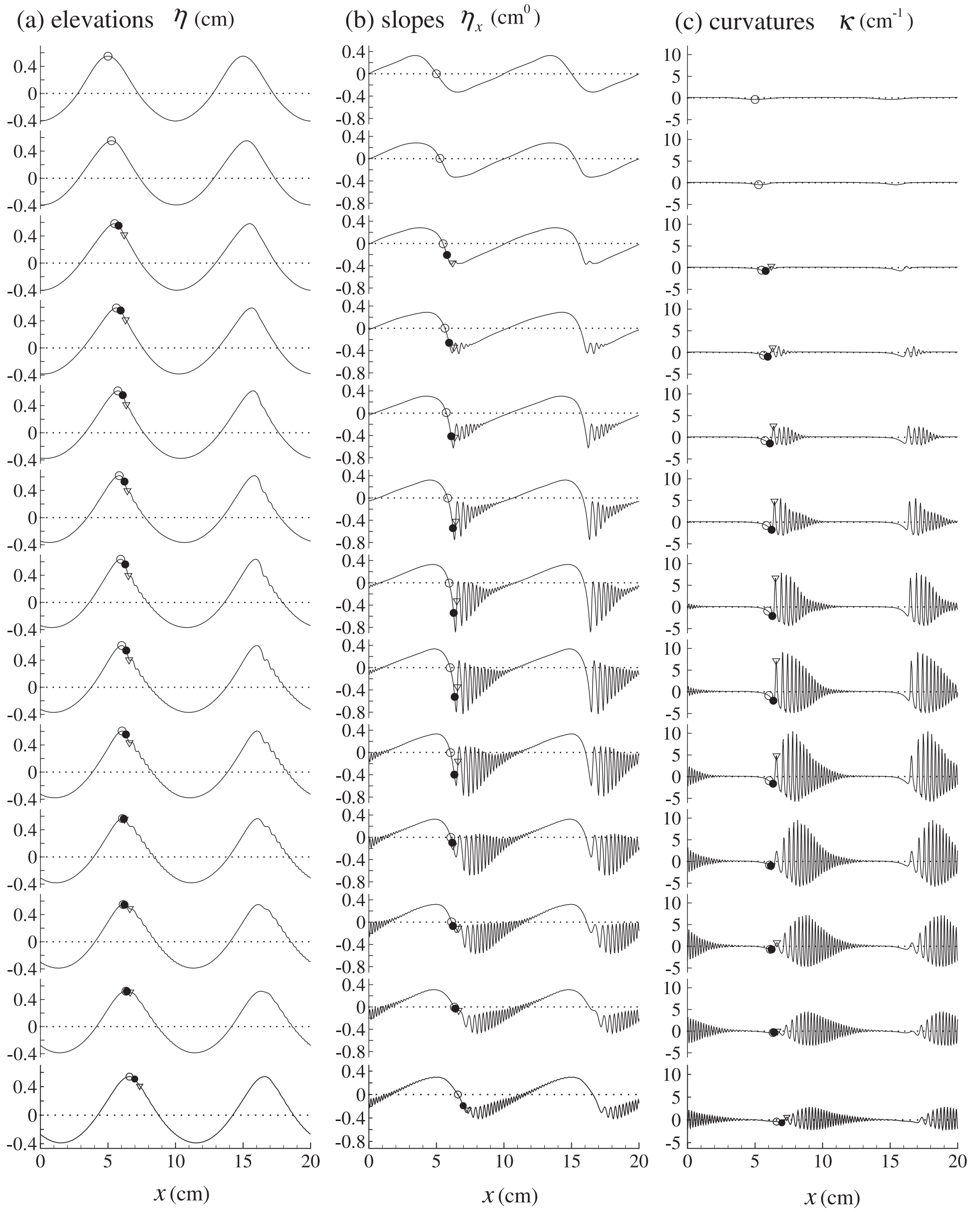

FIG. 4. As in Fig. 2, but the GCW with wavelength $\lambda = 10$ cm and initial steepness $a_0k = 0.3$.

simulations, respectively, where $T_0 = 2\pi(gk + \sigma k^3/\rho)^{-1/2}$ is the linear period of the GCW.

We also monitor the properties of mass and energy conservation in the computations. For all the simulated results presented in the following sections, the mean free surface is conserved to be within the machine precision ($k^2\int_0^\lambda \eta dx < 10^{-16}$), the error norm of the velocity divergence, $(gk)^{-1/2}\|\nabla \cdot \boldsymbol{v}\|_{L_2}$, is less than 10^{-10}, and the maximum velocity divergence, $(gk)^{-1/2}\|\nabla \cdot \boldsymbol{v}\|_{L_\infty}$, is less than 10^{-8}. The energy lost at the end of the simulation is only about 0.01% of the initial total energy, and the rate of relative energy loss due to numerical dissipation and errors remains at about 1% of the viscous dissipation.

3. Evolution of the surface waves

To reveal the formation process of the parasitic capillaries, we begin the presentation of the simulation results by first showing the cases where strong capillary ripples appear on the carrier GCWs in this section. Two representative examples of the surface evolution are shown in Figs. 2 and 3 for the GCW with wavelength

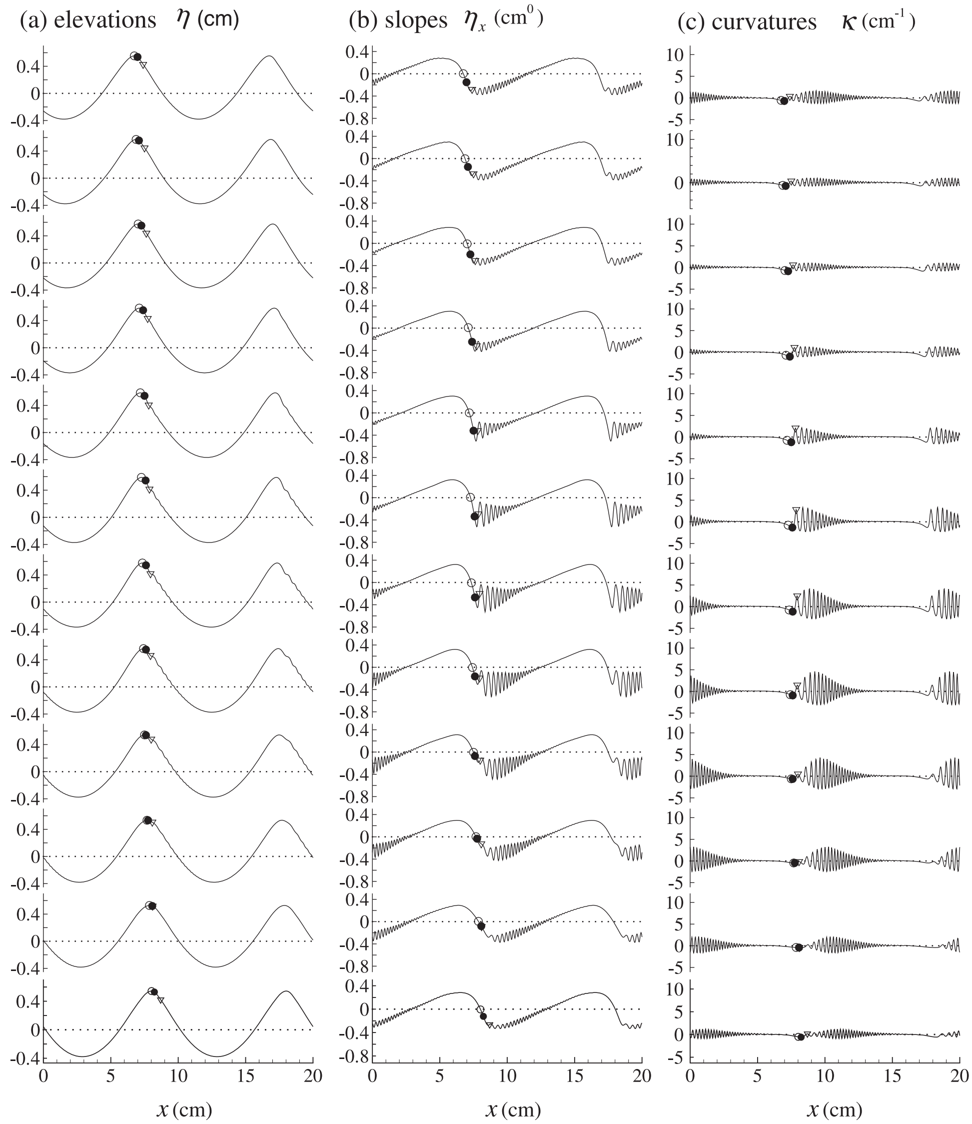

FIG. 5. As in Fig. 3, but for the consecutive evolution of surface profiles following that of Fig. 4.

$\lambda = 5$ cm and initial steepness $a_0k = 0.25$, and in Figs. 4 and 5 for $\lambda = 10$ cm and $a_0k = 0.3$. The various surface characteristics are exemplified by depicting the elevation η, the slope η_x and the curvature $\kappa = \eta_{xx}/(1 + \eta_x^2)^{3/2}$ in Figs. 2–5. The curvature is positive (negative) if the surface is concave (convex). To better reveal the surface variations, the periodic profile is repeated twice and the frame of reference moves with the linear phase speed $c_0 = (g/k + \sigma k/\rho)^{1/2}$. To elucidate the impact of surface tension, the corresponding evolution of a pure gravity wave of $\lambda = 5$ cm with vanishing surface tension ($\sigma = 0$) is also depicted in Fig. 6.

Since the simulation is started with a nonlinear progressive gravity wave, the initial surface elevation (slope) is symmetric (antisymmetric) with respect to the crest (and also the trough); and is flatter in the trough region and becomes sharper approaching the crest. The maximum convex curvature (negative) occurs right at the highest crest initially. (The instantaneous locations of the maximum elevation of the crest and the maximum convex are marked with open and solid circles, respectively, in the figures.) Note that there are no short-wavelength ripples riding on the initial GCW. As time proceeds, the crest skews forward and the shape of the surface elevation becomes considerably asymmetric as observed experimentally by Chang et al. (1978). The maximum convex curvature grows and moves away from the highest crest along the forward face of

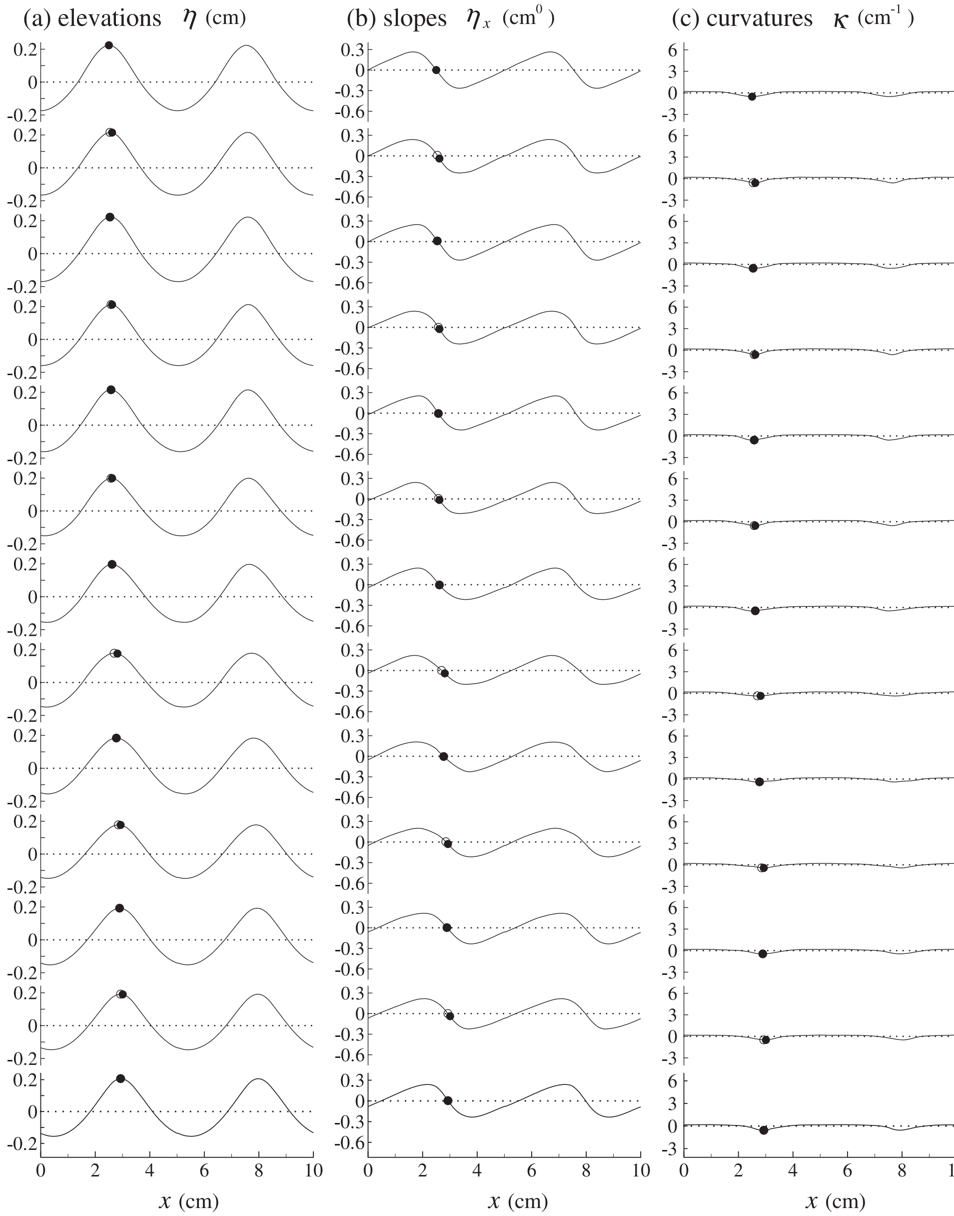

FIG. 6. Corresponding evolution of surface profiles of Fig. 2 ($\lambda = 5$ cm, $a_0k = 0.25$) of a pure gravity wave but with vanishing surface tension ($\sigma = 0$). The gravity wave propagates from left to right.

the carrier GCW (see, e.g., $t = 0.25T_0$ in Figs. 2 and 4). This leads to the formation of a ''bulge'' in the surface profile on the forward face of the carrier wave. Ahead of the bulge, a local maximum concave curvature (positive value, marked with an open triangle) occurs, which corresponds with the ''toe'' of the bulge (see $t = 0.5T_0$ in Figs. 2 and 4). Note that the present use of the terms bulge and toe is different from that in Duncan et al. (1994). The bulge and toe described by Duncan et al. (1994) are formed during an incipient wave-breaking process, which is a different process than the formation of bulge and toe in the steep GCWs without breaking.

As the GCW continues evolving, capillary ripples form from the toe and propagate downstream along the forward face of the dominant gravity wave (see $t \geq 0.75T_0$ in Figs. 2 and 4). Depending on the wavelength of the GCW, drastically different patterns of the capillary waves are observed. For the shorter GCW ($\lambda = 5$ cm), the process of generation and propagation of the capillaries continues, and the leading ripples of the capillary train even travel across the trough and reach the backward face of the next cyclic carrier wave (Figs. 2 and 3). For the longer GCW ($\lambda = 10$ cm), the amplitudes of the capillary waves decay quickly downstream from the crest, and the ripples appear as being trapped along the leading face of the GCW (Figs. 4 and 5). The generation of the capillary ripples eventually reaches a quasi-steady state (roughly after $t > 1.25T_0$ in Figs. 2 and 4), and the GCW profile consists of a capillary train with an approximately constant number of ripples riding on the dominant gravity wave. (The characteristic properties of the parasitic capillaries and their dependence on GCW wavelength and steepness will be discussed in section 4.) The amplitudes of the capillary ripples, however, undergo recursive modulation for both short and long GCWs. Since the frame of reference moves with the linear phase speed of the GCW, the shift of the location of the highest crest (marked with an open circle) downstream indicates a rise in the phase speed of the quasi-steady GCW.

In contrast to the GCW, no short-wavelength ripples appear on the pure gravity wave as shown in Fig. 6; the surface profiles remain similar to that of the initial Stokes wave and the evolution exhibits very minor decay in amplitude attributed to fluid viscosity. Such a contrast also implies the significance of surface tension in the formation of parasitic capillaries.

The first explanation for the generation of parasitic capillaries was given by Longuet-Higgins (1963). The theory argues that the parasitic capillaries are attributed to the perturbation in the pressure brought about by the localized surface tension near the crest of the gravity wave, where the curvature is relatively large. Viewed in a reference frame moving with the phase velocity, the wave appears as a current flowing in the opposite direction of the wave propagation. The localized pressure near the crest then produces ripples upstream of the crest; that is, on the forward face of the carrier wave. The theory was confirmed by the experiments of Chang et al. (1978) and Ermakov et al. (1986), and improved in Longuet-Higgins (1995).

To demonstrate the physical explanation of Longuet-Higgins, distributions of the total pressure $p_t = p - \rho g \eta$, where p is the hydrodynamic pressure, during the initial development of parasitic capillaries are shown in Fig. 7. The distributions clearly reveal a localized action of pressure on the initial crest (Fig. 7a) and the leading slope near the crest of the GCW (Figs. 7b–e).

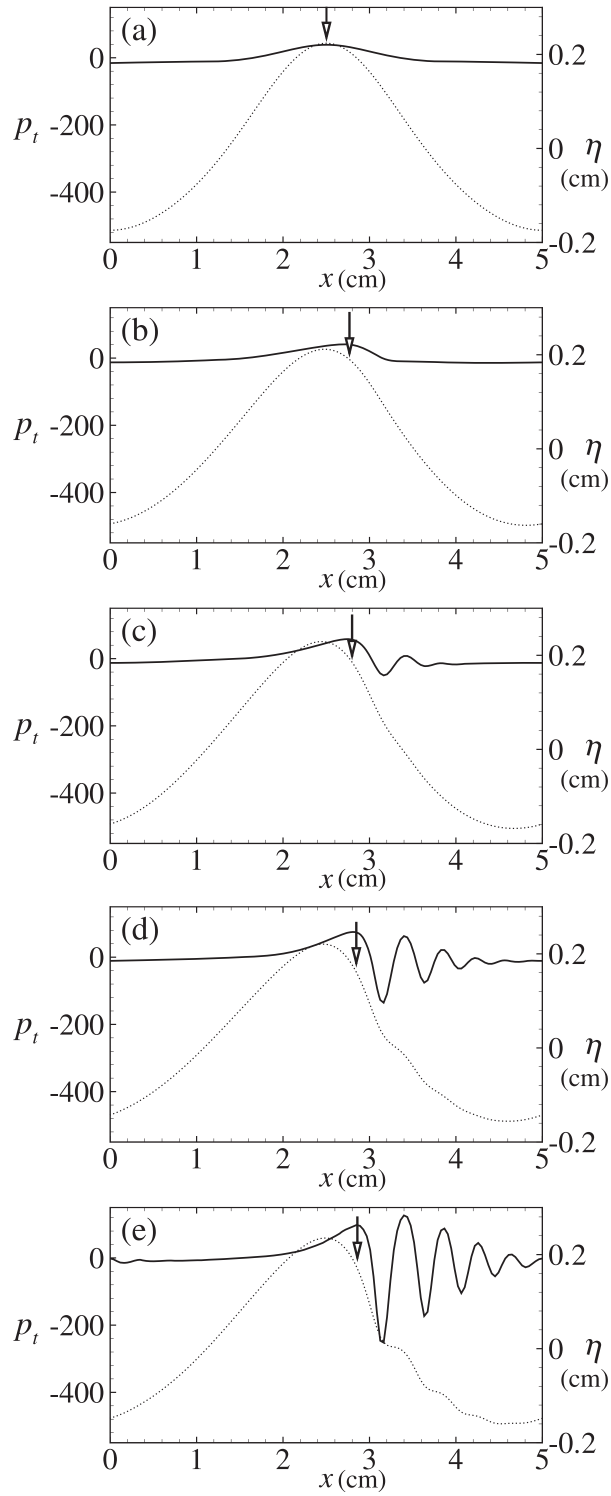

FIG. 7. Total pressure distributions (solid curves) p_t (dyne cm^{-2}) on the water surface during the initial development of parasitic capillary ripples at (a) $t = 0$, (b) $T_0/4$, (c) $T_0/2$, (d) $3T_0/4$, and (e) T_0. The GCW wavelength $\lambda = 5$ cm and the initial steepness $a_0k = 0.25$. The dotted curves are the corresponding surface profiles. The GCW propagates from left to right. The vertical arrows indicate the locations of local pressure maxima.

4. Characteristics of parasitic capillaries

Previous experimental studies (e.g., Ermakov et al. 1986; Fedorov et al. 1998) and theoretical analyses (e.g., Ruvinsky et al. 1991; Fedorov and Melville 1998)

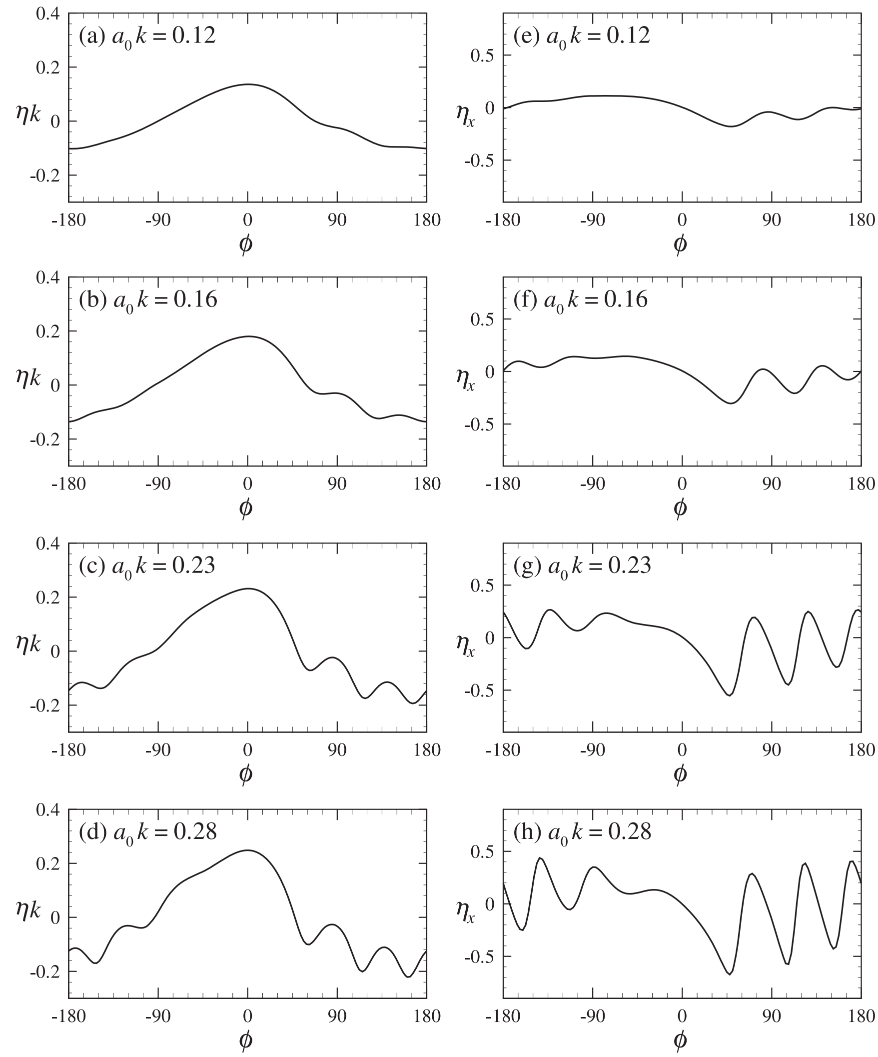

FIG. 8. Profiles of (a)–(d) surface elevations and (e)–(h) slopes at $t = 2T_0$ for GCW wavelength $\lambda = 3.9$ cm and various initial GCW steepnesses: $a_0k =$ (a),(e) 0.12; (b),(f) 0.16; (c),(g) 0.23; and (d),(h) 0.28. The profiles have been shifted such that phase angle of the highest crest is $\phi = 0$. The GCW propagates from left to right.

indicate that the appearance of parasitic capillaries on a GCW is very sensitive to the wavelength and steepness of the GCW. To reveal such a dependency, instantaneous surface elevations and slopes (at $t = 2T_0$) of GCWs with $\lambda = 3.9$, 5, 7, and 10 cm are shown in Figs. 8–11, respectively, for various steepnesses. The qualitative characteristics of the parasitic capillaries observed in the present numerical simulations are identical to the previous experimental and theoretical findings: when the parasitic capillary train forms along the surface of the GCW, both the wavelengths and the amplitudes of the capillary ripples decrease along the forward surface. For a particular GCW wavelength, the steepness of the parasitic capillaries increases with that of the GCW; however, the wave patterns, including the total number and the wavelengths of the ripples, are independent of the GCW steepness.

A salient difference between the shorter ($\lambda = 3.9$, 5, and 7 cm) and the longer ($\lambda = 10$ cm) GCWs, as discussed in section 3, can be observed from these simulation results. For the shorter waves, the capillary ripples distribute along the entire surface of the GCW (Figs. 8–10); while for longer waves, the amplitudes of the capillary ripples decay rapidly and the visible ripples are trapped on the forward face of the GCW (Fig. 11). Such a feature was also noticed in the experiments of Ermakov et al. (1986) and Fedorov et al. (1998). We, however, do not observe the instability near the crest of the GCW,

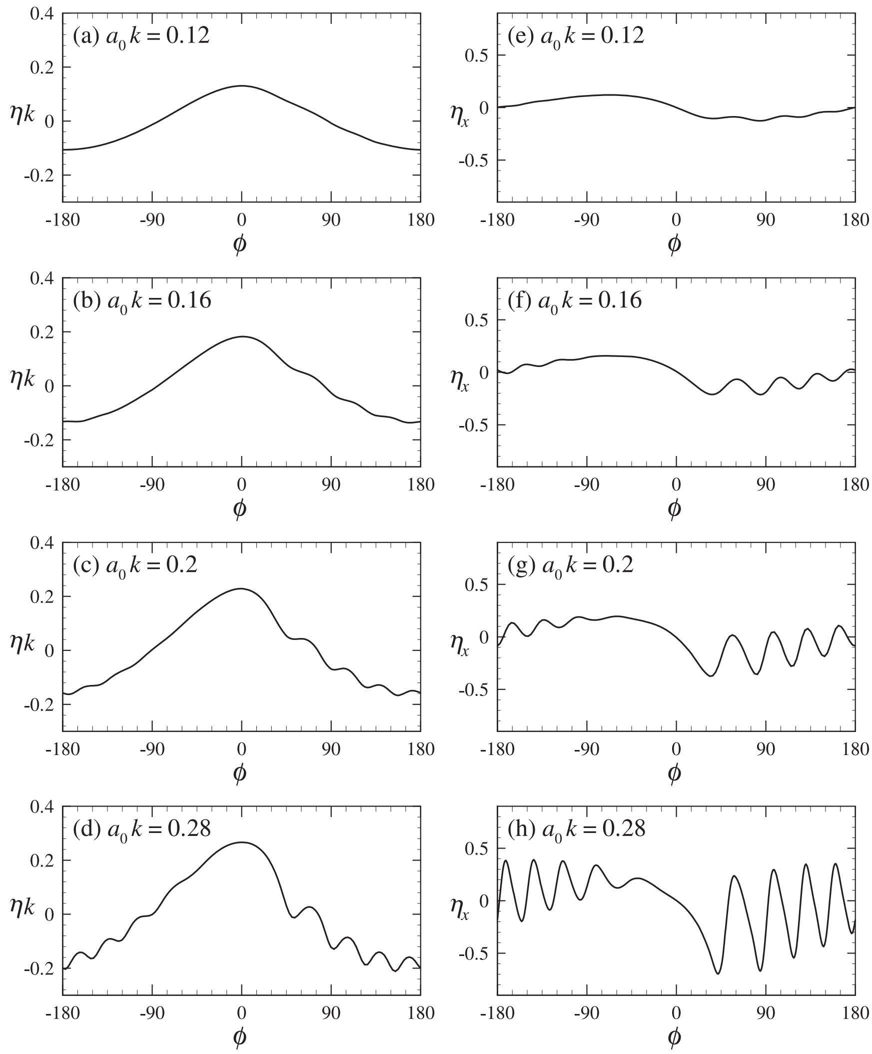

FIG. 9. As in Fig. 8, but for GCW wavelength $\lambda = 5$ cm and various initial GCW steepnesses: $a_0k =$ (a),(e) 0.12; (b),(f) 0.16; (c),(g) 0.2; and (d),(h) 0.28.

which appears as irregular capillary ripples as reported by Fedorov et al. (1998). Fedorov et al. (1998) postulated that such irregularity in the capillary ripples might be due to modulational instability of the underlying GCWs at these amplitudes and wavelengths.

As noted in section 3, the evolution of the GCWs and their formation of parasitic capillaries are transient in the present simulations. This is similar to the waves observed in the laboratory experiments (e.g., Ermakov et al. 1986; Fedorov and Melville 1998). Consequently, the amplitude of the simulated GCW attenuates slowly with time, and the appearance of the parasitic capillaries can only be considered as quasi-stationary. Figure 12, showing the temporal evolution of the carrier wave height H for $\lambda = 3.9$, 5, 7, and 10 cm, and various initial steepnesses a_0k, depicts such a temporal decay. Comparison among the results of various initial steepnesses reveals an important property that a steeper GCW, of which the amplitudes of parasitic capillaries are also larger, possesses a greater decaying rate. As such, a steeper GCW can continue to attenuate with time, and its wave height may eventually decreases to be less than those GCWs with lower steepnesses (e.g., see $\lambda = 3.9$ cm and $a_0k = 0.25$ in Fig. 12a, $\lambda = 5$ cm and $a_0k = 0.28$ in Fig. 12b, and $\lambda = 7$ cm and $a_0k = 0.3$ in Fig. 12c). Such a feature also implies the efficiency of the parasitic capillary ripples in dissipating the GCW energy.

To further quantify the characteristics of the parasitic capillary ripples and their temporal evolution, two properties of the ripples are computed from our numerical results and compared with those by theoretical analyses and/or experimental measurements. Figure 13

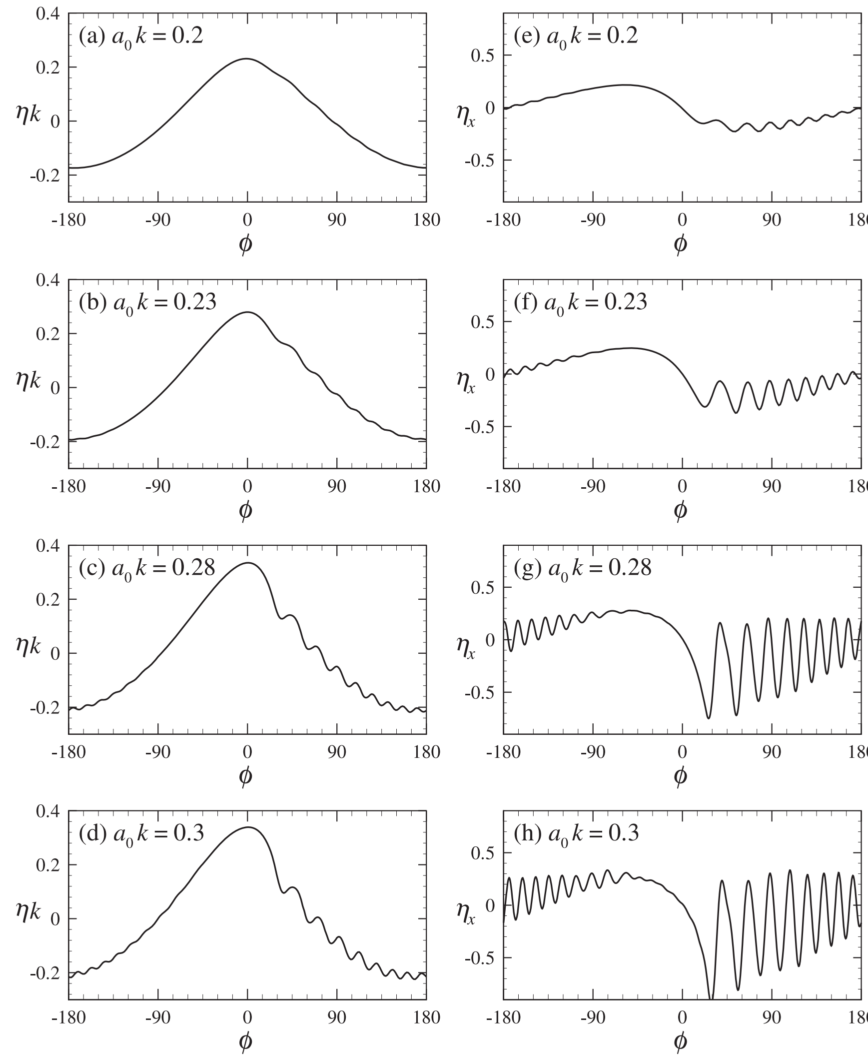

FIG. 10. As in Fig. 8, but for GCW wavelength $\lambda = 7$ cm and various initial GCW steepnesses: $a_0k =$ (a),(e) 0.2; (b),(f) 0.23; (c),(g) 0.28; and (d),(h) 0.3.

shows temporal evolution of the average steepness of the first capillary ripple θ_r on the forward face of the GCW for wavelengths $\lambda = 3.9$, 5, 7, and 10 cm, and various initial steepnesses a_0k. Following Ermakov et al. (1986), the average steepness of the first ripple θ_r is defined as $\theta_r = 0.5(\theta_{\max} - \theta_{\min})$, as illustrated in Fig. 14, where $\theta_{\max}$ and $\theta_{\min}$ are the maximum and minimum slopes, respectively, along the ripple surface. The GCWs are initiated without any capillary ripples in the numerical simulations; as soon as the capillary ripples are excited, the average steepness of the first capillary θ_r increases rapidly with time. The steepness reaches its maximum and then decreases to a minimum. The process of amplification and attenuation of the capillary steepness repeats, and the parasitic capillaries exhibit a modulating pattern as depicted in Figs. 2–5. The modulation period is almost invariant with carrier GCW steepness and wavelength; and is approximately 3 times the linear carrier wave period (approximately 0.43, 0.51, 0.62, and 0.76 s for $\lambda = 3.9$, 5, 7, and 10 cm, respectively). Such temporal modulation over times of $O(1)$ s was also observed in the experiment of Fedorov et al. (1998). They noticed that the undulating unsteadiness becomes more substantial for longer GCWs, in agreement with the present numerical results. The origins of this recurrence phenomenon and the parameters controlling the modulation period, however, are still unclear, and deserve further investigation. It appears that the modulational instability of the carrier GCW cannot be the appropriate process to explain it because the time scale is very short, and this modulation is particularly well pronounced for waves of scale as small as $\lambda = 3.9$ cm

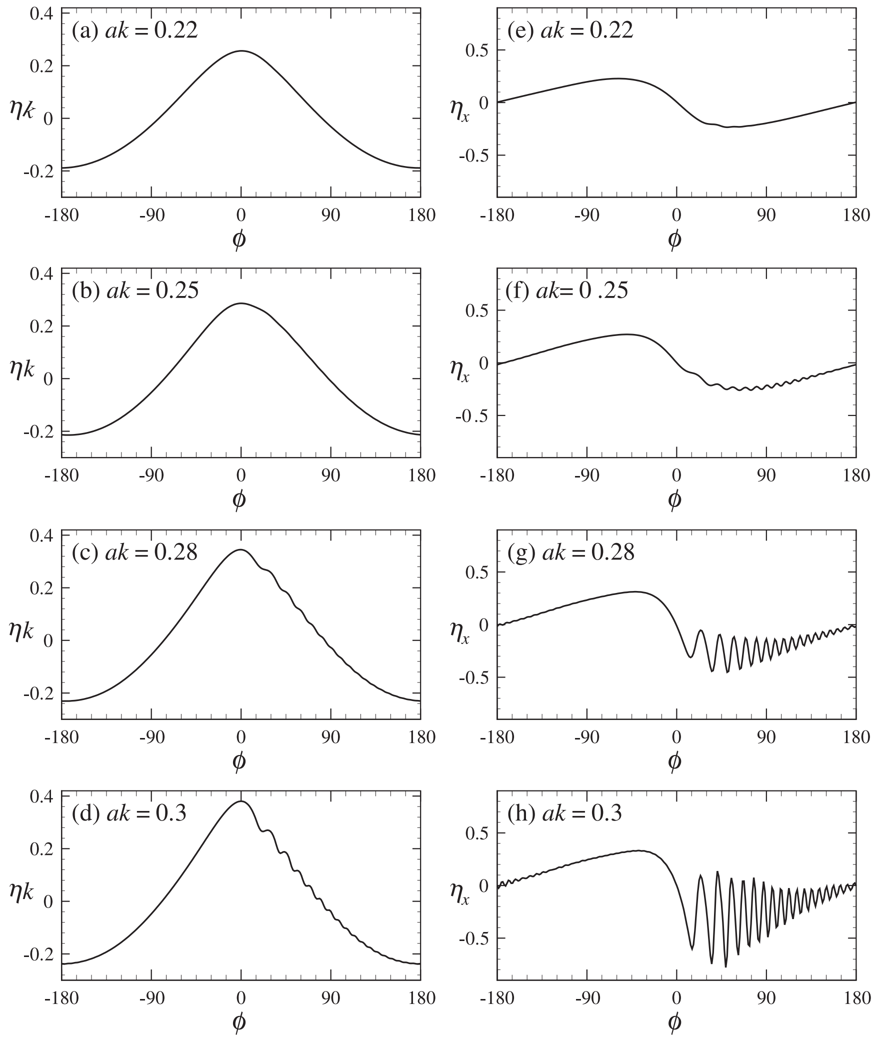

FIG. 11. As in Fig. 8, but for GCW wavelength $\lambda = 10$ cm and various initial GCW steepnesses: $a_0k =$ (a),(e) 0.22; (b),(f) 0.25; (c),(g) 0.28; and (d),(h) 0.3.

[the analysis of Hogan (1985) indicates that instability is impossible in a range of $0.155 < \kappa_\sigma < 0.5$, corresponding to 2.43 cm $< \lambda <$ 4.36 cm, where the dimensionless capillary number $\kappa_\sigma = 4\pi^2\sigma/\rho g\lambda^2$]. Thus, it is feasible that such a recurrent modulation is caused by the nonlinear interaction between the carrier GCW and the parasitic capillary ripples.

A direct comparison of the average ripple steepness θ_r between the present numerical results and the experimental measurements of Ermakov et al. (1986) and Fedorov et al. (1998) is shown in Fig. 15. Since both θ_r and ak change with time, the transient numerical results are averaged over the interval from $t = T_0$ to $4T_0$. The chosen averaging interval is roughly the modulation period of the average ripple steepness θ_r as shown in Fig. 13. The numerical results provide good quantitative agreement with the experimental measurements for the entire steepness range of λ = 3.9-, 5-, and 7-cm GCWs. Larger deviations, however, occur for the longer GCW of $\lambda = 10$ cm.

The results of characteristic capillary steepness θ_r depicted in Figs. 13 and 15 reveal that there exists a minimum critical steepness of the GCW for the formation of visible parasitic capillaries; and such a critical steepness increases with the GCW wavelength. The present numerical results also confirm the finding of Ermakov et al. (1986) that ripple excitation can initiate with a relatively small GCW steepness 4–5 times less than that of the maximum steepness of GCW. Since the formation of capillary ripples on a steep GCW is due to the development of local pressure anomaly near the GCW crest, the existence of this minimal GCW steepness can be linked to a threshold in the magnitude of such pressure disturbance. Furthermore, pressure distribution on the

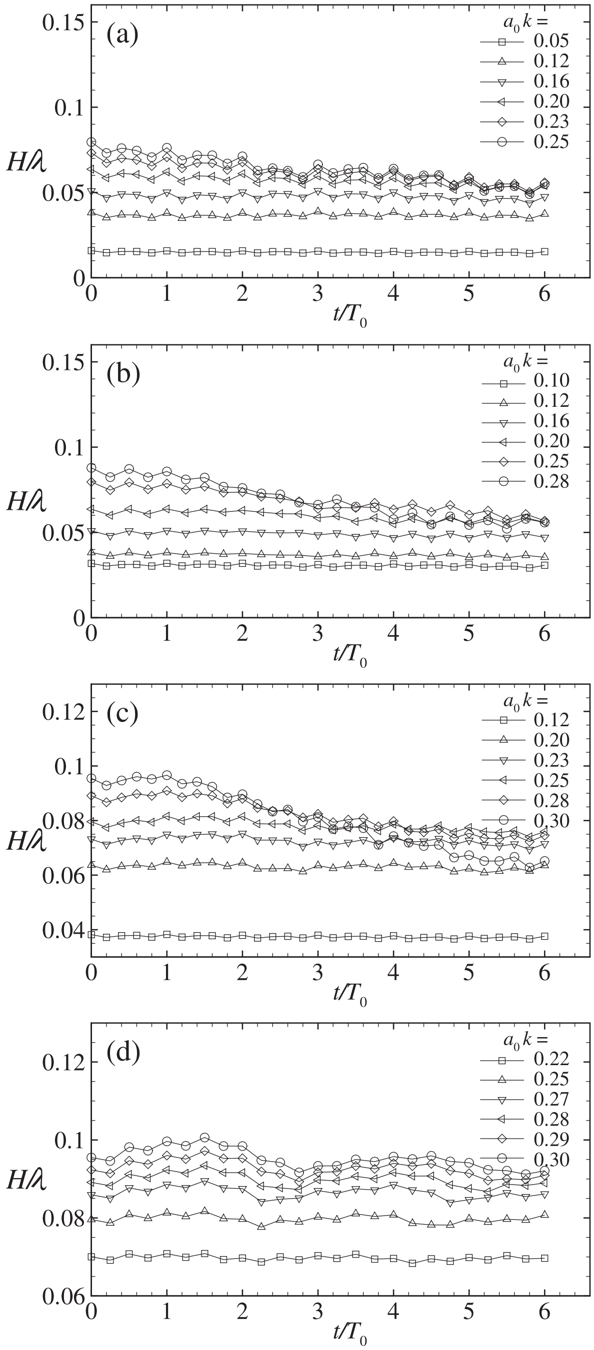

FIG. 12. Temporal evolution of the nondimensional wave height H/λ of the GCWs for λ = (a) 3.9, (b) 5, (c) 7, and (d) 10 cm, and various initial steepnesses a_0k as shown in the figures. The GCW wave height H is defined as the difference between the maximum and minimum surface elevations.

water surface is predominantly balanced by surface-normal component of the surface tension, $\sigma\kappa$. As such, this localized pressure perturbation can be evaluated by surface curvature k at the GCW crest. To reveal the possible correlation between the minimal GCW steepness and the critical GCW crest curvature for the formation of capillary ripples, the dependence of crest curvature κ on initial steepness a_0k for various GCW wavelengths is shown in Fig. 16. The appearance of parasitic capillaries on a carrier GCW is identified if the averaged capillary steepness θ_r is higher than 0.002 at any time of the evolution as shown in Fig. 13. The GCW steepness, which forms capillary ripples, is marked with a solid symbol in Fig. 16. The result clearly indicates that there exists a minimal GCW crest curvature, almost independent of the wavelength of the carrier wave, for the formation of capillary ripples on the carrier GCW. Such a threshold curvature is estimated to be 0.25 cm^{-1} from our systematic numerical experiments. The corresponding critical initial steepnesses a_0k for ripple initiation are approximately 0.12, 0.14, 0.18, and 0.24 for GCW wavelengths λ = 3.9, 5, 7, and 10 cm, respectively. This finding also supports the previous laboratory observation of Ermakov et al. (1988) that the condition for generation of capillary ripples on a GCW is governed solely by the crest curvature of the GCW.

Temporal evolution of the wavelength of the first capillary on the forward face of the GCW next to the crest, λ_r, for various GCW wavelengths λ and initial steepnesses a_0k is shown in Fig. 17. The capillary wavelength λ_r is defined as the distance between the first and second slope maxima, as illustrated in the schematic of Fig. 14. In contrast to the ripple steepness θ_r, the temporal variation of wavelength λ_r is minimal for the ranges of GCW wavelength and steepness considered. The capillary ripples are shorter for longer GCWs as revealed in Fig. 18. Comparisons of λ_r between the present numerical results and the measurements by Ermakov et al. (1986) and Fedorov et al. (1998) are depicted in Fig. 18, which also show quantitative agreement for the ranges of wavelength and steepness considered. For a constant GCW wavelength, the capillary wavelength decreases slightly with the increasing GCW steepness. Such a dependency on GCW steepness, however, is not as significant as that of capillary steepness (Fig. 15).

The temporal evolution of the number of parasitic capillary ripples N_p riding along the GCW for λ = 3.9, 5, 7, and 10 cm, and various initial steepnesses a_0k is shown in Fig. 19. The number of capillary ripples is determined by counting the numbers of local minimum slopes, as depicted in Figs. 8–10. Since the simulations are initiated without any prescribed capillary ripples, the number of capillary ripples increases rapidly when the steepness of the gravity capillary wave reaches the critical value for ripple generation. For the GCWs of λ = 3.9, 5, and 7 cm, the number of ripples N_p eventually reaches a constant level with small variations as the carrier wave evolves;

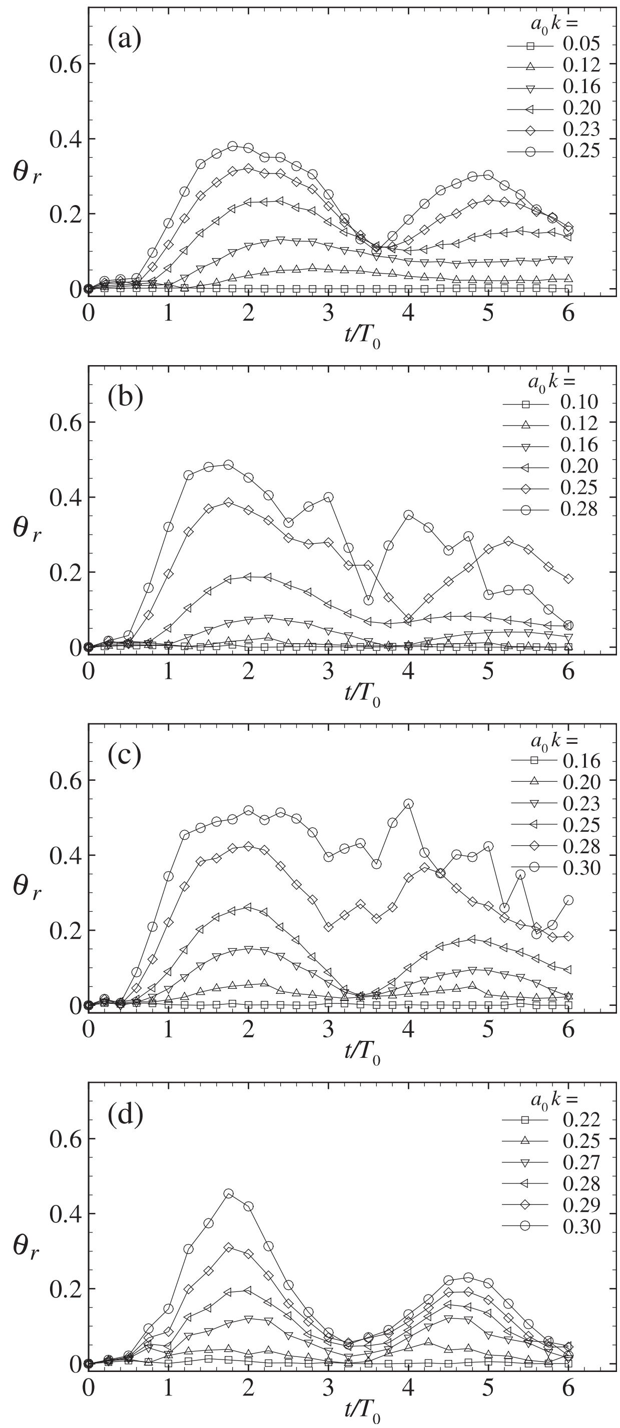

FIG. 13. Temporal evolution of the average steepness θ_r of the capillary ripple on the forward face and immediately next to the crest of the GCW for λ = (a) 3.9, (b) 5, (c) 7, and (d) 10 cm, and various initial steepnesses a_0k as shown in the figure. The average steepness θ_r is defined as the schematic depicted in Fig. 14.

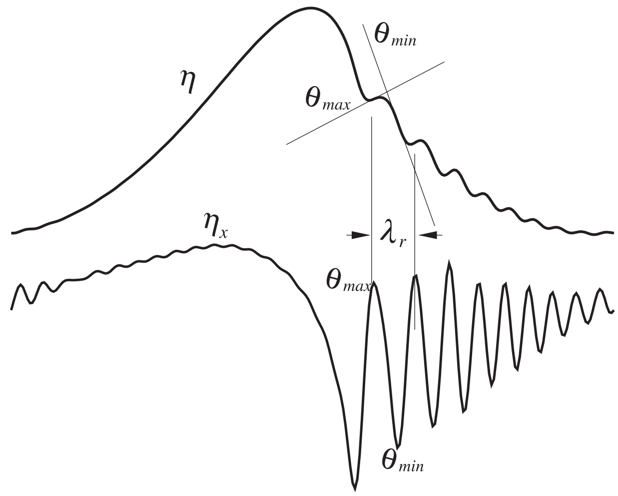

FIG. 14. A schematic illustrating the definitions of θ_r and λ_r. Following Ermakov et al. (1986), the average steepness of the capillary ripple on the forward face of the GCW immediately next to the crest, θ_r, is defined as $\theta_r = 0.5(\theta_{\max} - \theta_{\min})$, where $\theta_{\max}$ and $\theta_{\min}$ are the maximum and minimum slopes along the ripple surface, respectively. The wavelength λ_r is defined as the distance between the first and second horizontal coordinates with the local maximum slopes.

and the number of ripples increases with the GCW wavelength λ, but is not affected by the initial steepness a_0k. For the GCW of λ = 10 cm, however, the ripple number $N_p$modulates significantly with time.

The number of parasitic ripples can also be estimated by assuming constant wavelengths of the ripples λ_p and from the resonance condition that the linear phase speed of the GCW matches that of the parasitic capillary ripples (Cox 1958; Fedorov and Melville 1998): $N_p \approx \lambda/\lambda_p = \rho g\lambda^2/4\pi^2\sigma$. For the GCWs of wavelengths λ = 3.9, 5, 7, and 10 cm, the estimated numbers of parasitic capillaries are N_p = 5, 8, 16, and 34, respectively. The results are close to that from the present simulations (Fig. 19).

5. Underlying flow structures

The corresponding flow structures underneath the GCWs of Figs. 2 and 3 (λ = 5 cm) and Figs. 4 and 5 (λ = 10 cm) are depicted in Figs. 20 and 21 , respectively. The instantaneous distributions of velocities (u and w) and vorticity ($\omega = \partial u/\partial z - \partial w/\partial x$) at various stages of the wave evolution are also plotted in a reference frame moving with the linear phase speed. The distribution of the flow field at the initial stage of the simulation is dominated by that of the gravity wave, but begins to skew toward the forward face of the carrier wave (see $t = 0.25T_0$ in Figs. 20a,e,i and 21a,e,i). Note that a thin layer of counterclockwise vortices (negative vorticity, in blue) is observed immediately beneath the crest of the carrier wave, and clockwise vortices underneath the trough (Figs. 20i and 21i).

As the wave evolves, capillary wavelets begin to form on the forward slope near the GCW crest and interfere with the gravity-dominant carrier wave. However, completely different flow structures are observed underneath the shorter (λ = 5 cm) and longer (λ = 10 cm) GCWs. For the case of λ = 5 cm, the perturbations induced by the parasitic capillary waves on the underlying velocity field grow significantly as the capillary wave train develops (Figs. 20c,g). The magnitudes of the perturbed velocities eventually surpass those of the carrier wave and dominate the GCW velocity field (Figs. 20d,h). (Note that the pattern of the velocity field induced by an individual capillary ripple is similar to that induced by the dominant gravity wave.) In contrast, for the GCW with λ = 10 cm, the velocities attributed to the gravity wave are still the prevailing components in the velocity field (cf. Figs. 21a and 21b–d; cf. Figs. 21e and 21f–h). At the stage when parasitic capillaries are fully developed, the riding ripples only cause minimal velocity disturbances confined within a shallow region beneath the forward slope of the carrier wave (Figs. 21d,h).

Accompanying the generation of parasitic capillary ripples on the forward slope of the carrier GCW, vortical layers with alternate vorticity orientations are observed to form immediately underneath the capillary wave train (Figs. 20j and 21j). Each vortical layer with positive (clockwise) vortices shed from the capillary trough is accompanied by a neighboring, negative (counterclockwise) vortical region, which has formed underneath the capillary crest; and the vorticity strength of the trough vortical layer is stronger than that of the neighboring crest vortices. Both the vorticity strength and the thickness of these alternate vortical layers decay away from the GCW crest along the forward surface. Such a vortical structure, with weak, counterclockwise vortices underneath the capillary crest and strong, clockwise vortices shed from the trough, is quantitatively consistent with the previous simulation result of Mui and Dommermuth (1995) and also the experimental

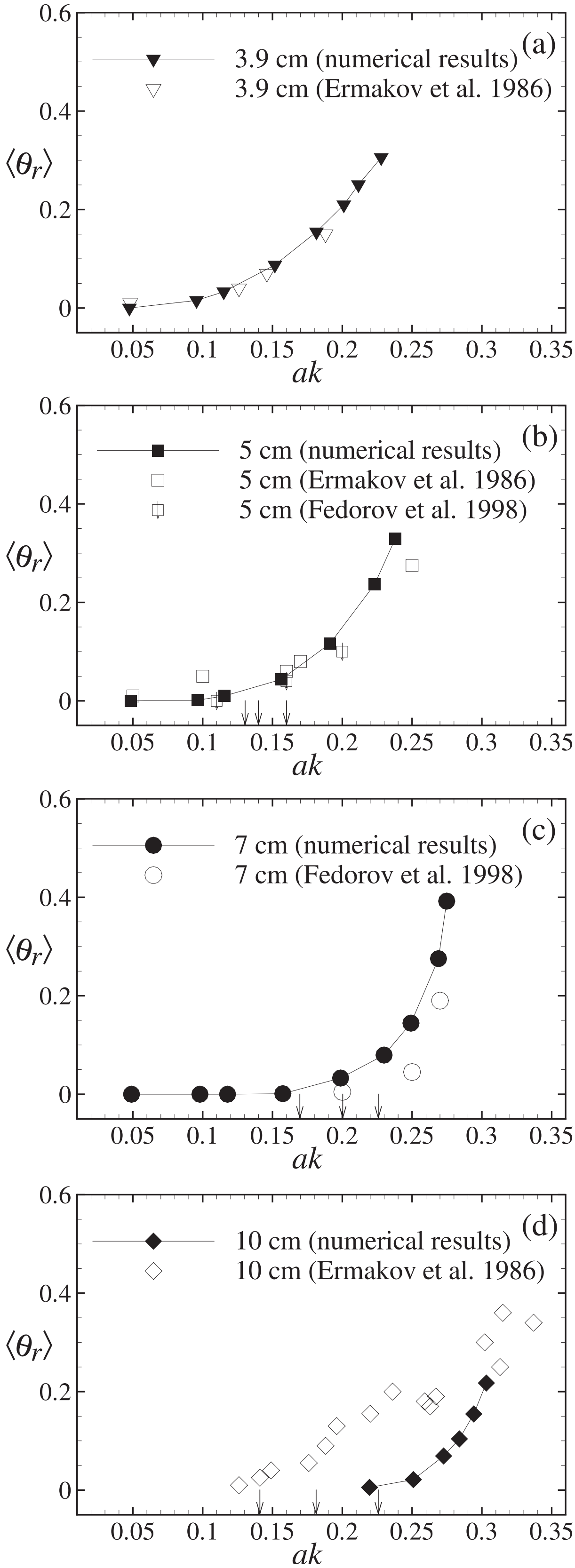

←

FIG. 15. Comparisons between the present numerical simulations and the experimental measurements of Ermakov et al. (1986) and Fedorov et al. (1998) for the temporal-averaged steepness θ_r of the capillary ripple on the forward face and immediately next to the crest of the GCW. The steepnesses of the carrier GCW considered in the experiment of Lin and Perlin (2001) (ak = 0.13, 0.14, and 0.16 for $\lambda \approx$ 5 cm; ak = 0.17, 0.2, and 0.225 for $\lambda \approx$ 7 cm; ak = 0.14, 0.18, and 0.225 for $\lambda \approx$ 10 cm) are marked with arrows in the ak axes: λ = (a) 3.9, (b) 5, (c) 7, and (d) 10 cm.

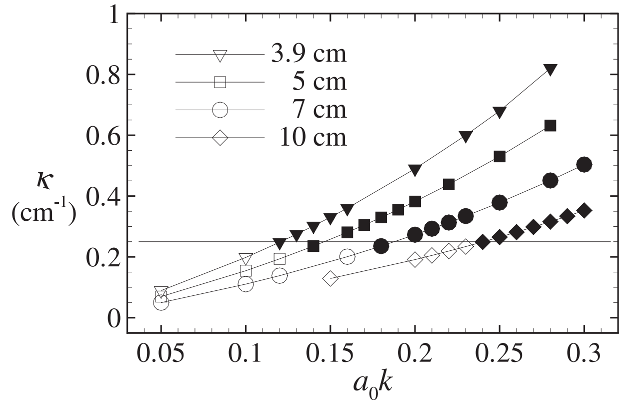

FIG. 16. Dependence of crest curvature κ on initial steepness a_0k for GCW wavelength $\lambda = 3.9$, 5, 7, and 10 cm. The pair of GCW steepness and crest curvature, which results in capillary ripples is marked with a solid symbol, and the open symbol represents parameter with no capillaries formed. The estimated threshold crest curvature ($\approx 0.25\ \mathrm{cm}^{-1}$) is marked with a horizontal line.

observations of Lin and Rockwell (1995) and Lin and Perlin (2001). Similar to the distribution of velocity field, the deepening of the vortical layers induced by the parasitic capillaries is more pronounced in a shorter GCW than in a longer GCW (the thickness of the shear layer underneath the GCW crest is about 2.5% of the GCW wavelength in Fig. 20 and is about 1.5% in Fig. 21).

The structure of the vortical layers shown in Fig. 20k can be further elucidated from the velocity distributions in Figs. 20c,g. The velocity distribution of an individual parasitic capillary ripple is similar to that of the dominant gravity wave: pronounced forward (backward) horizontal velocities are observed underneath the crest (trough); and upward (downward) vertical velocities underneath the forward (backward) face of the ripple surface. Accordingly, underlying a capillary ripple, the strong vortical layer generated from the trough is convected backward and lifted up along the forward surface of the ripple crest behind, forming a vortex shedding wake; and the accompanying weak vorticity region beneath the crest is stretched toward the backward ripples' surface.

As the parasitic capillary waves continue developing, both the strength and the thickness of the underlying vortical layers grow, and the regions extend toward the GCW crest. The vortical layers shed from the capillary troughs outgrow those developing beneath the capillary crests (Figs. 20k and 21k). These outgrowing vortical layers with clockwise vortices eventually become connected, and form the predominant vortical structure underneath the carrier GCW, as shown in Figs. 20l and 21l. The extended region of such a predominant vortical layer covers the entire GCW crest. This strong vortical region

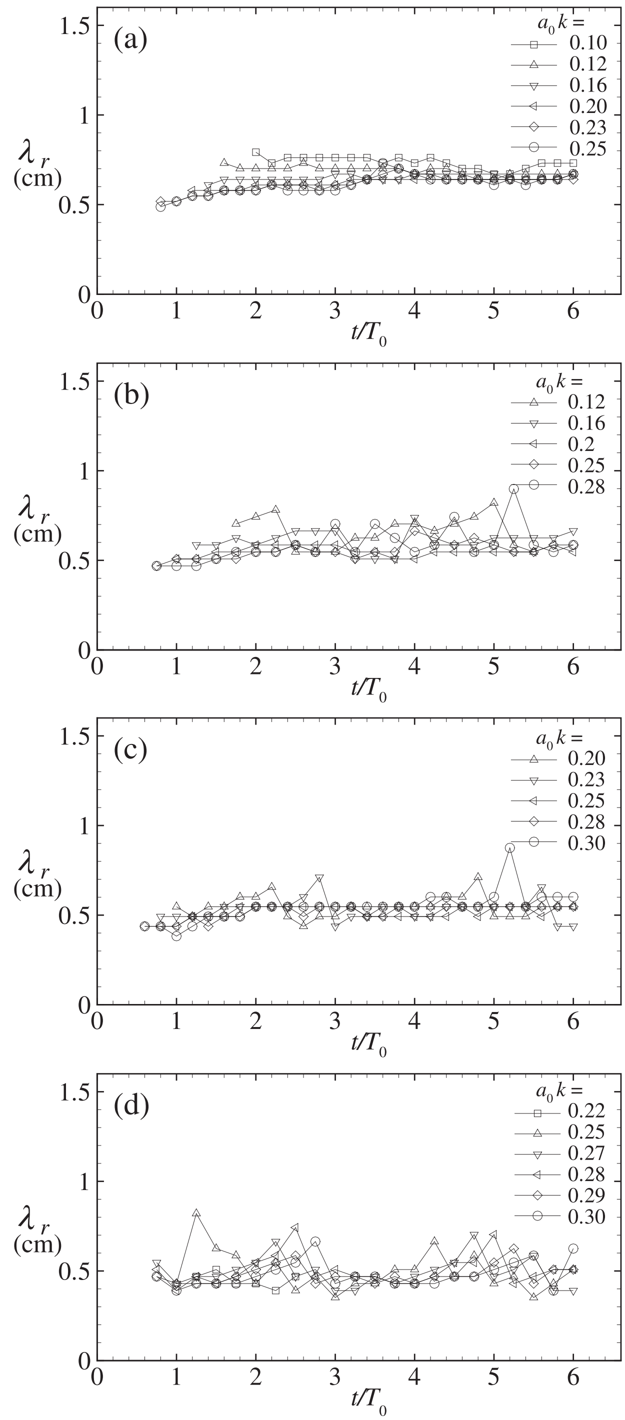

FIG. 17. Temporal evolution of the wavelength λ_r (cm) of the capillary ripple on the forward face and immediately next to the crest of the GCW for λ = (a) 3.9, (b) 5, (c) 7, and (d) 10 cm, and various initial steepnesses a_0k as shown in the figure. The capillary wavelength λ_r is defined as shown in Fig. 14.

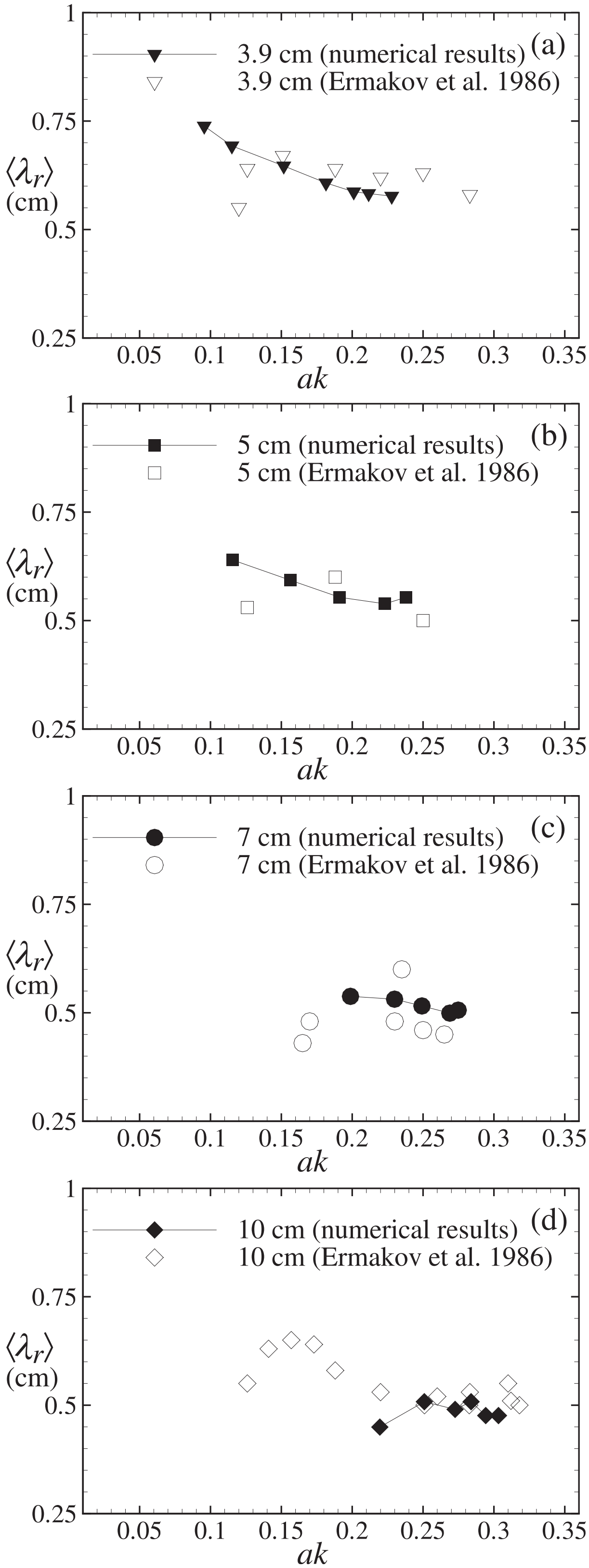

underneath the entire crest of the GCW resembles the "capillary rollers" pointed out by Longuet-Higgins (1992, see their Fig. 12). The present simulation therefore confirms the postulate of Longuet-Higgins (1992) that the source of this crest vortical roller can be from the parasitic capillaries on the forward face of a GCW. The vortices are shed from the capillaries ahead of the GCW crest attributed to the large curvatures of the capillary troughs. These vortices then flow back and accumulate mainly underneath the crest of the dominant gravity wave. Our numerical experiment further indicates that as the GCW wavelength increases, the strength of the vortical layer shed underneath the parasitic capillaries weakens, and its thickness and extent reduce. The vortices accumulated within the GCW crest, therefore, are not as pronounced as the crest roller of the shorter GCWs (cf. Figs. 20l and 21l).

Such a vortex shedding process is further revealed in Fig. 22 by correlating the vorticity distributions to their corresponding vorticity transport rates at two representative times when the capillaries just arise ($t = T_0$; Figs. 22a–c) and when the capillaries fully develop ($t = 2T_0$; Figs. 22d–f). In Fig. 22, the coordinate moves with the instantaneous phase velocity c of the GCW; and the resulting flow corresponds to a backward flow with a freestream velocities $-c$. The transport rates of vorticity attributed to convection and diffusion, accordingly, are $-[(u - c)\partial\omega/\partial x + w\partial\omega/\partial z]$ and $\nu\Delta^2\omega$, respectively.

The distributions of the vorticity transports are similar at both instances when the capillaries just arise and fully develop. Strong diffusion transport is observed near the vicinity of individual ripple trough where the maximum vorticity influx occurs (see the next section and Fig. 23). The wake of the concave region of positive diffusion is followed by a convex region of intensified convection transport. Such a region with strong, positive convection extends toward the submerged area beneath the neighboring ripple crest. The shed vortices near the capillary troughs are therefore convected toward the crest and form the observed strong vortical structure beneath the crest.

6. Vorticity interaction with the surface

The underlying vorticity field discussed in the previous section is generated by the surface deformation and

←

FIG. 18. Comparisons between the present numerical simulations and the experimental measurements of Ermakov et al. (1986) for the temporal-averaged wavelength λ_r (cm) of the capillary ripple on the forward face and immediately next to the crest of the GCW: λ = (a) 3.9, (b) 5, (c) 7, and (d) 10 cm.

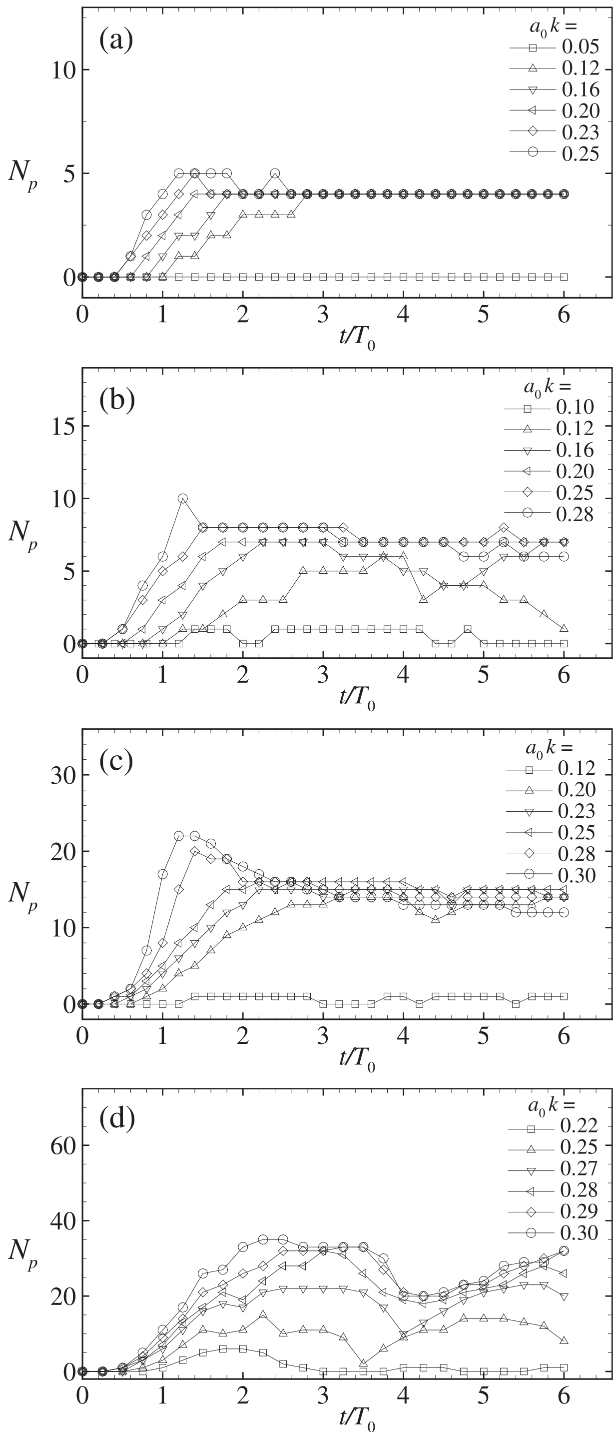

FIG. 19. Temporal evolution of the number of parasitic capillary ripples N_p riding along the GCW for λ = (a) 3.9, (b) 5, (c) 7, and (d) 10 cm, and various initial steepnesses a_0k as shown in the figure.

motion of the capillary ripples. The surface vorticity [$\omega_0 = \omega(z = \eta)$] on an unsteady free-surface boundary can be derived from the balance condition of tangential stresses and expressed as (Wu 1995)

$$\omega_0 = -2\frac{\partial u_n}{\partial s} - 2ku_s, \tag{1}$$

where s is the tangential curvilinear coordinate along the surface, and u_s and u_n are the tangential and the normal velocities on the surface, respectively. The distributions of surface vorticity calculated from the numerical simulation and the theoretical expression in (1) are shown in Fig. 23 for the corresponding time intervals of Figs. 20 and 22. The maximum relative error between the numerical and theoretical results is less than 2%, implying the capability of the present model in accurately satisfying the dynamic free-surface boundary conditions and in resolving the capillary ripples. The variations of surface vorticity (Figs. 23b,e,h,k) well correlate with that of surface curvatures (Figs. 23a,d,g,j). The vorticity strengths on the ripple troughs are greater than those on the ripple crests, which is consistent with the underlying vorticity field discussed in the previous section. Also plotted in Figs. 23b,e,h,k are the steady and linear approximation of the free-surface vorticity (Longuet-Higgins 1995): $\omega_0 \approx 2\kappa c_0$. Only small deviations from the unsteady, nonlinear values are observed, indicative of minimal effects of the unsteadiness and the nonlinearity of the base flow (the carrier GCW).

To further reveal the production sources of the underlying vortices, the vorticity flux at the free surface is then examined. For a two-dimensional vortical flow, the processes of vortex stretching and tilting are absent; viscous diffusion is the only mechanism governing vorticity transport. The rate of vorticity transport in a two-dimensional flow can be expressed as

$$\iiint_{\mathcal{V}} \frac{D\omega}{D\omega} d\mathcal{V} = \iiint_{\mathcal{V}} \upsilon\nabla^2\omega d\mathcal{V} = \iint_{S} \upsilon\frac{\partial\omega}{\partial n} dS, \tag{2}$$

where Gauss's theorem has been used to convert the volume integral to a surface integral, and the surface normal vector $\mathbf{n}$ points outward. The physical meaning of Eq. (2) is that the net rate of vorticity change within the flow is balanced by the flux of vorticity diffusing across the free surface as a result of viscous forces. The diffusion flux of vorticity across the free surface can be further expressed in a curvilinear coordinate system along the surface (s,n) as (Rood 1995; Gharib and Weigand 1996):

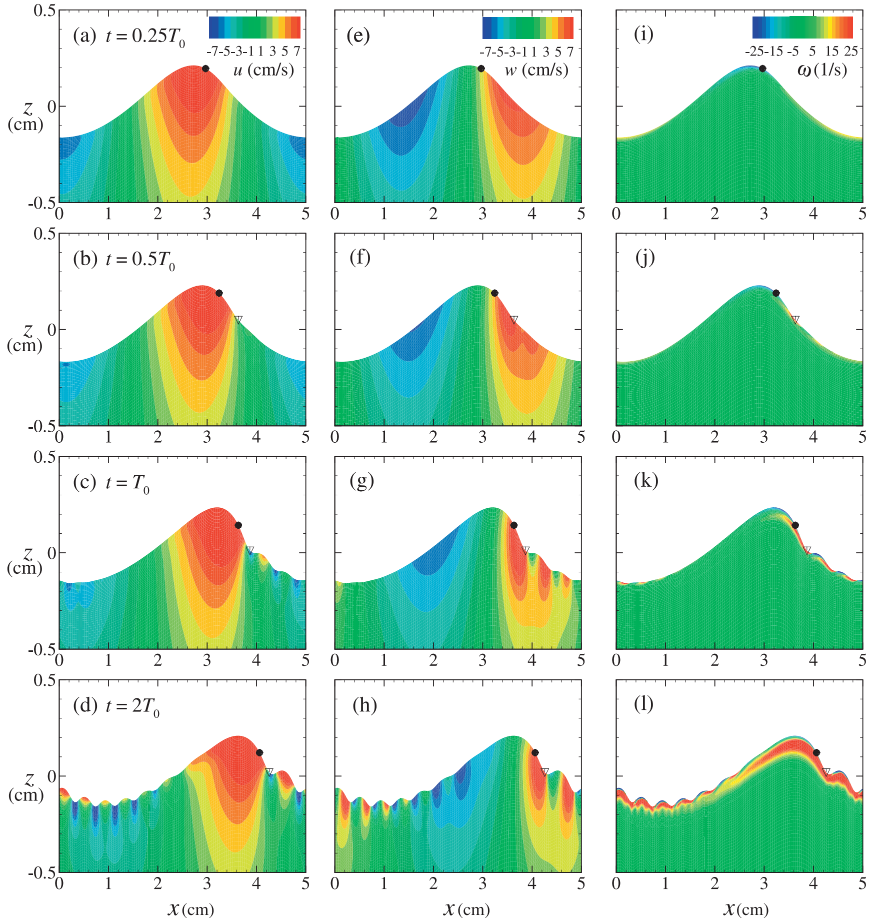

FIG. 20. Instantaneous distributions of (a)–(d) horizontal velocity u (cm s^{-1}), (e)–(h) vertical velocity w (cm s^{-1}), and (i)–(l) vorticity ω (1 s^{-1}) for GCW wavelength $\lambda = 5$ cm and initial steepness $a_0k = 0.25$ at $t =$ (a),(e),(i) $0.25T_0$; (b),(f),(j) $0.5T_0$; (c),(g),(k) T_0; and (d),(h),(l) $2T_0$. The positions of the bulge and toe are marked with a solid circle and triangle, respectively. The GCW propagates from left to right.

$$-\nu\left(\frac{\partial\omega}{\partial n}\right)_{n=0} = -\frac{\partial u_s}{\partial t} - \left(u_s\frac{\partial u_s}{\partial s} + u_n\frac{\partial u_n}{\partial s} + u_n\omega\right) - \frac{1}{\rho}\frac{\partial p}{\partial s} - g\cos\theta, \tag{3}$$

where θ is the angle of the surface with respect to the gravity vector. Equation (3) is derived by projecting the momentum equation onto the surface tangent. It decomposes the total vorticity influx $[-\nu(\partial\omega/\partial n)_{n=0}]$ into contributions from local acceleration $(-\partial u_s/\partial t)$, convective accelerations $(-u_s\partial u_s/\partial s - u_n\partial u_n/\partial s - u_n\omega)$, pressure gradient $(-\rho^{-1}\partial p/\partial s)$, and gravity $(-g\cos\theta)$.

The distributions of the total vorticity influx at the free surface and its contributing components are shown in Figs. 23c,f,i,l. The contribution by local acceleration (dashed lines) to the vorticity flux is very weak throughout the entire wave evolution. At the initial stage when the gravity wave dominates the base flow and the capillary ripples have not developed, both the surface vorticity and the vorticity flux are weak (Figs. 23b,c); the surface vorticity production is dominated by the gravitational effect (dashed–dotted line). At the time when localized surface tension triggers the formation of capillary ripples, the effects of convective acceleration (dashed–dotted–dotted line) and pressure gradient (solid line) on the vorticity flux become as significant as that attributed to gravitation (Fig. 23f). At the time when parasitic capillary waves become fully developed, the variation of the dominant contribution by pressure gradient (and also the total vorticity influx) is well correlated with the distribution of parasitic capillaries as shown in Figs. 23i,l. The inward vorticity flux attributed to the pressure gradient is positive on the forward face of capillaries, and negative on the leeward face. The pressure gradient effect, therefore, dominates the vorticity production by the parasitic capillary ripples.

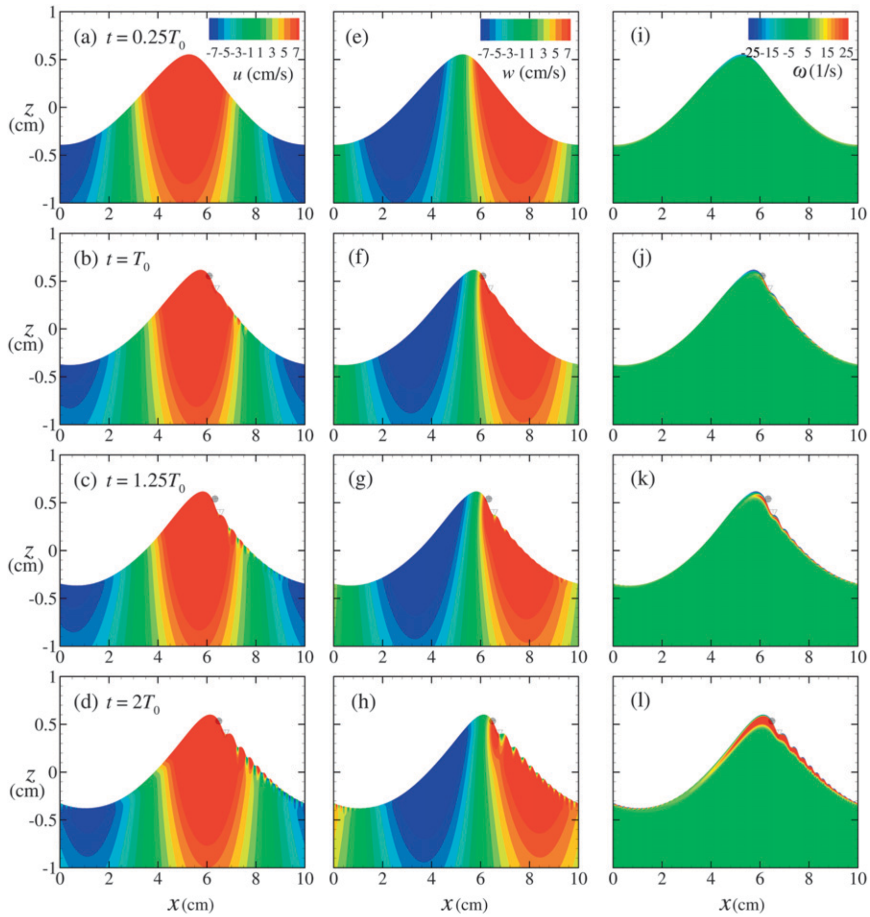

FIG. 21. As in Fig. 20, but for GCW wavelength $\lambda = 10$ cm and initial steepness $a_0k = 0.3$ at $t =$ (a),(e),(i) $0.25T_0$; (b),(f),(j) $0.5T_0$; (c),(g),(k) T_0; and (d),(h),(l) $2T_0$.

7. Discussion

The generation and evolution of parasitic capillary ripples on gravity–capillary waves are studied numerically by solving the initial–boundary–value problem of a free-surface flow. Two distinct features of the present computations are the following: 1) The complete free-surface boundary conditions are satisfied on the deformable water surface without any approximation or linearization. As such, the nonlinear dynamics involved in the formation of parasitic capillary waves and their interactions with the underlying flow are modeled by the first-principle formulation. 2) The numerical model implements a spectrally accurate scheme for the horizontal discretization and adopts stretched finer grids approaching the water surface. Accordingly, the model is capable of resolving surface wavelets of the capillary scale and the underlying flow with length scale down to the viscous sublayer immediately next to the wavy surface. Our simulation result shows good quantitative agreements of the capillary characteristic properties (i.e., steepness, wavelength, number of wavelets) with the measurements of Ermakov et al. (1986) and Fedorov et al. (1998), which validate the use of the model to explore the formation mechanism and the underlying flow structure of the parasitic capillary waves.

Our simulation results confirm the generation mechanism originally proposed by Longuet-Higgins (1963) that the initial capillary wavelets are triggered by the combined effect of pressure from localized surface tension forces on the forward slope near the crest and the underlying current attributed to phase translation of the carrier wave. Force exerted by wind is not necessary for the formation of capillary ripples, and the source of energy for parasitic capillary waves is the carrier GCW itself. Systematic numerical experiments reveal that the crest curvature of the carrier GCW is the major parameter governing the occurrence of the parasitic capillaries. There exists a minimum crest curvature of the GCW for the formation of parasitic capillary ripples;

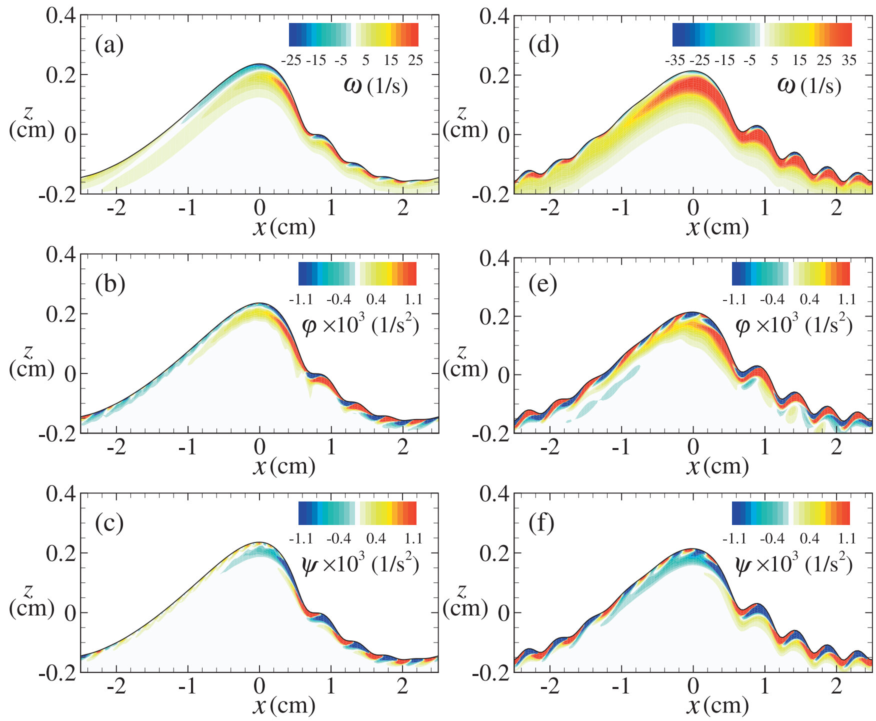

FIG. 22. Instantaneous distributions of (a),(d) vorticity ω (s^{-1}); (b),(e) vorticity transport rate of vorticity due to convection $-[(u-c)\partial\omega/\partial x + w\partial\omega/\partial z] \equiv \varphi$ (s^{-2}); and (c),(f) vorticity transport rate due to diffusion $\nu\nabla^2\omega \equiv \psi$ (s^{-2}) for GCW wavelength $\lambda = 5$ cm and initial wave steepness $a_0k = 0.25$ at $t =$ (a)–(c) T_0 and (d)–(f) $2T_0$.

and such a threshold curvature ($\approx$0.25 cm^{-1}) is almost independent of the carrier wavelength.

Note that in parallel with the present numerical computation concerning the dynamical evolution of nonsymmetric GCWs, there are also theoretical analyses (e.g., Chen and Saffman 1979; Hogan 1980) and numerical solutions (e.g., Chen and Saffman 1980; Schwartz and Vanden-Broeck 1979) of steady symmetric GCWs of finite amplitude. These studies show the multiplicity of solutions due to resonant interactions of waves leading to bifurcations between different continuous families of solutions, and indicate the exceptional complexity even in the symmetric GCWs of permanent form. Among other phenomenon, the theoretical analysis made by Chen and Saffman manifests that the solution bifurcation due to resonant interactions between the fundamental and the Nth harmonic waves can result in the formation of $N - 1$ capillaries along the surface of the basic wave. The present numerical results also reveal strong evidence that nearly resonant nonlinear interactions play a major role in the formation of parasitic ripples. This is supported by at least two facts: 1) the wave profile reaches a quasi-steady state after a transient regime certainly controlled by the initial conditions; and 2) the number of capillary ripples N_p observed strikingly checks the resonant condition that the linear phase velocity of the GCW matches that of the parasitic capillaries.

Both the characteristics of the parasitic capillaries and the underlying vortical structures exhibit strong sensitivity to the wavelength of the carrier GCW. For shorter GCWs (wavelength approximately less than 10 cm), the parasitic capillary wave train is distributed over the entire surface of the carrier wave. The leading ripple of the capillary wave train can even pass through the rear face of the adjacent crest, and interfere with the tail ripples (the ripples on the forward face and immediately next to the crest). In contrast, for longer GCWs, the amplitudes of the parasitic capillary wave train decay rapidly, and the capillary ripples appear as being trapped on the forward face between the crest and the trough. Such distinct features of the parasitic capillary wave trains on shorter and longer GCWs can be attributed to the wave energy propagation and thus, to the respective values of the parasitic ripple group velocity and the carrier wave phase speed. The linear phase velocity of the gravity-dominant carrier wave is proportional to $\lambda^{1/2}$, whereas the linear group velocity of the capillary ripple is proportional to $\lambda_r^{-1/2}$. As revealed in Figs. 17 and 18, the wavelength of the parasitic capillaries decreases slightly

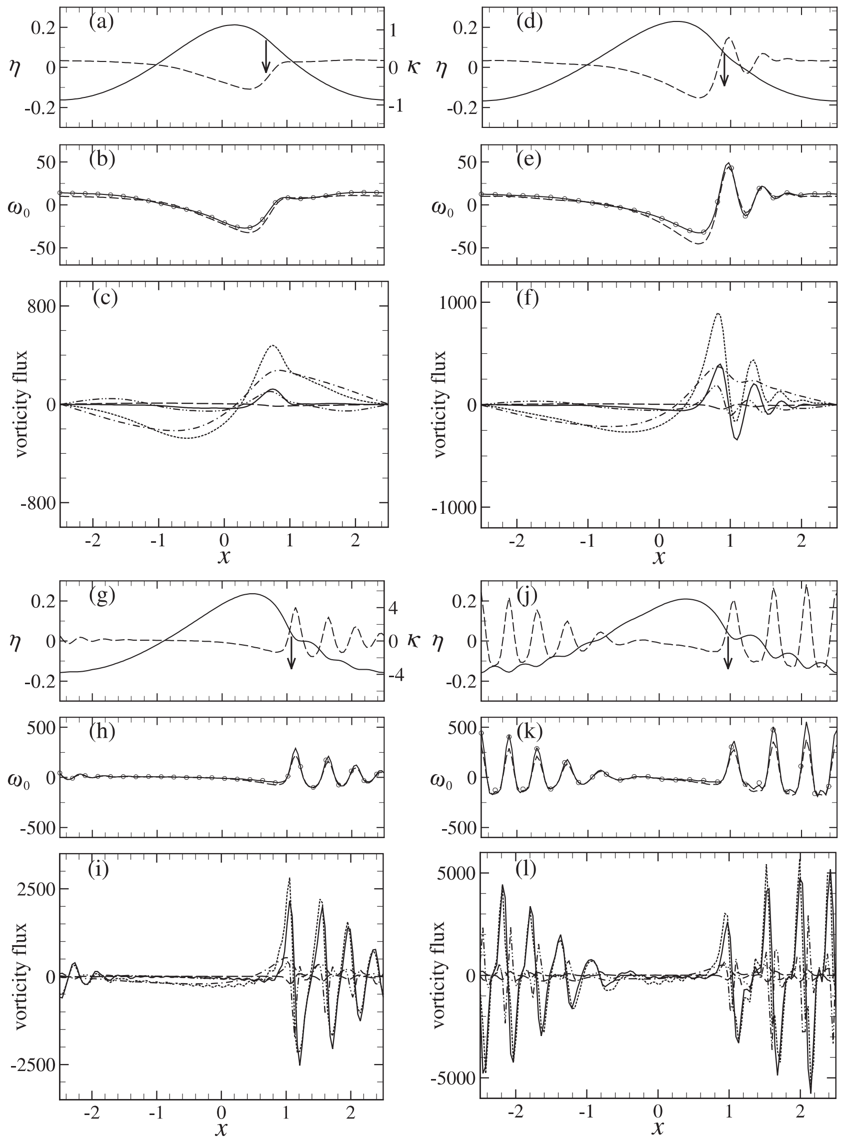

FIG. 23. Distributions of (a),(d),(g),(h) surface elevation η (solid lines, cm) and curvature κ (dashed lines, cm^{-1}); (b),(e),(h),(k) surface vorticity ω_0 from numerical simulation (solid lines, in s^{-1}) and theoretical prediction of Eq. (1) (open circles, s^{-1}), and steady, linear approximation (dashed lines, in s^{-1}); (c),(f),(i),(l) vorticity influx (dotted lines, $\mathrm{cm}^{-1}\ \mathrm{s}^{-1}$), and the separated components in Eq. (3): the local acceleration term (dashed lines, $\mathrm{cm}^{-1}\ \mathrm{s}^{-1}$), the convective acceleration term (dashed–dotted–dotted lines, $\mathrm{cm}^{-1}\ \mathrm{s}^{-1}$), the pressure gradient term (solid lines, $\mathrm{cm}^{-1}\ \mathrm{s}^{-1}$), and the gravity term (dashed–dotted lines, $\mathrm{cm}^{-1}\ \mathrm{s}^{-1}$) for GCW wavelength $\lambda = 5$ cm and initial steepness $a_0k = 0.25$ at (a)–(c) $t = 0.25T_0$; (d)–(f) $0.5T_0$; (g)–(i) T_0; and (j)–(l) $2T_0$. The vertical arrows in (a), (d), (g), and (j) indicate the horizontal positions where the maximum vorticity influxes occur.

as the wavelength of the carrier GCW increases and so does the group velocity of the capillary; while on the contrary, the carrier wave propagates faster (slower) when its wavelength increases (decreases). When the carrier wave wavelength increases above a certain value, it turns out immediately that the phase velocity of carrier gravity component can be in excess of the group velocity of the parasitic capillaries riding on the orbital velocity of the gravity component, and the capillary wave train energy can never catch up with the propagation of the carrier GCW; the capillary ripples, however, continue being generated along the forward face of the GCW. As such, the capillary wave train appears to be blocked on the forward face between the crest and the trough. While on the contrary, when the phase velocity of a shorter GCW is lower than that of the group velocity of capillary waves, the capillary wave train can propagate over the entire surface of the carrier wave.

Similar to surface distribution of the parasitic capillaries, the underlying velocity and vorticity fields also exhibit distinctive patterns depending on the GCW wavelength. At the time when parasitic capillaries are fully developed, both the velocity and the vorticity fields of a shorter GCW are overtaken by that induced by the capillary ripples. In particular, an enhanced vortex layer is formed within the surface boundary layer. The vortices shed from the troughs of the capillary ripples prevail in the vortical layer, and are convected toward the GCW crest to form the observed crest roller, in support of the analysis of Longuet-Higgins (1992). In contrast to the shorter GCWs, the vortices generated underneath the parasitic capillaries become weaker as the GCW wavelength increases, and the accumulated crest roller is less significant. These findings, however, seem to contradict the previous numerical simulation of Mui and Dommermuth (1995) and the measurements of Lin and Perlin (2001). The explanations for these contrary conclusions are as follows.

Both Mui and Dommermuth (1995) and Lin and Perlin (2001) considered free-propagating GCWs without the action of wind stresses, as in the present numerical study. To reduce the computation time for solving the Navier–Stokes equations of a viscous flow, Mui and Dommermuth (1995) spun up their simulation by assuming irrotationality of the initially developing flow and adopting a faster potential solver up to the time when the capillary wave train forms on the carrier GCW ($t \approx 1.8T_0$). The subsequent simulation was then switched to a Navier–Stokes solver for a fraction of the period of the GCW ($\approx 0.136T_0$). This means that they have only simulated the processes of vortex shedding from the parasitic capillaries and the transport for a very short time interval. Our numerical result indicates that it would take about a GCW period ($\approx T_0$, see Fig. 20) for the shed vortex layer to fully develop and to be convected to the GCW crest. This explains why Mui and Dommermuth (1995) have not observed a strong vortical structure underneath the GCW crest in their simulation ($\lambda = 5$ cm, $a_0k = 0.2827$).

Lin and Perlin (2001) conducted particle image velocimetry (PIV) measurements of velocity fields beneath GCWs with wavelengths $\lambda = 5, 7$, and 10 cm. But, in comparison with the previous experiments, the steepness of the GCWs considered by Lin and Perlin (2001) ($ak = 0.13, 0.14$ and 0.16 for $\lambda \approx 5$ cm; $ak = 0.17$, 0.2, and 0.225 for $\lambda \approx 7$ cm; $ak = 0.14, 0.18$, and 0.225 for $\lambda \approx 10$ cm) is relatively much lower (for comparison, these steepnesses are marked with arrows in Fig. 15). We have also conducted simulations within the range of these steepnesses (see Fig. 15); the strong vorticity regions underneath the moderate-steep GCW crests are not realized in the numerical simulations, in agreement with the experimental results of Lin and Perlin (2001).

Okuda (1982) measured the internal velocity distributions of wind-generated waves with wavelengths ranging from 10 to 15 cm. He argued that the occurrence of the high-vorticity region near the crest is associated with a large local tangential wind stress on the windward face near the crest of the carrier wave. [Such a feature was also pointed out by Ebuchi et al. (1987), who used the same wind–wave flume as in the experiment of Okuda (1982) did.] The analysis of Longuet-Higgins (1992) suggested that the direct effect of the wind stress in producing the crest vorticity is small, compared with that generated by the parasitic capillaries. The present numerical simulation, however, indicates that for the GCW of $\lambda \approx 10$ cm the vorticity generated by the presence of parasitic capillaries alone is not strong enough to retain a crest roller with a significant extent.

To manifest the possibility that wind shear stress can be a source of near-surface vorticity comparable to that of parasitic capillaries, numerical simulations of the $\lambda =$ 10-cm GCW subject to a shear stress imposed at the water surface are also conducted. Two types of shear stress distributions τ_t^s, are considered: the distribution measured by Okuda (1982, see his Fig. 7) and the more recent measurement of Banner and Peirson (1998, see their Fig. 5). Figure 24 depicts two instantaneous distributions of the surface profiles and the underlying vorticity field plotted following the style of Fig. 3 in Okuda (1982). For comparison the results of the free-propagating GCW are also plotted in Fig. 24. Note that parasitic capillary ripples are barely visible for the free-propagating GCW of $\lambda = 10$ cm with an initial steepness $a_0k = 0.23$ as shown in Figs. 24a,b, and also indicated by the experiment of Lin and Perlin (2001). Vertical distributions of vorticity below the crest and the trough of the carrier GCW at various times are depicted in Fig. 25. As expected, the exerting shear stress induces a strong vortical layer immediately underneath the backward surface of the GCW at the early stage of the wave development when the formation of parasitic capillaries is still not significant (Figs. 24c,e). This surface stress induced vortical layer is convected backward beneath the rear slope of the carrier wave, and becomes submerged underneath the trough (Figs. 25d,f). The wind stress, nevertheless, enhances the generation of capillary ripples as the wave continues evolving as shown in Figs. 24d,f; and vortical layers form underneath these capillaries and intensify the vorticity region in the crest. The

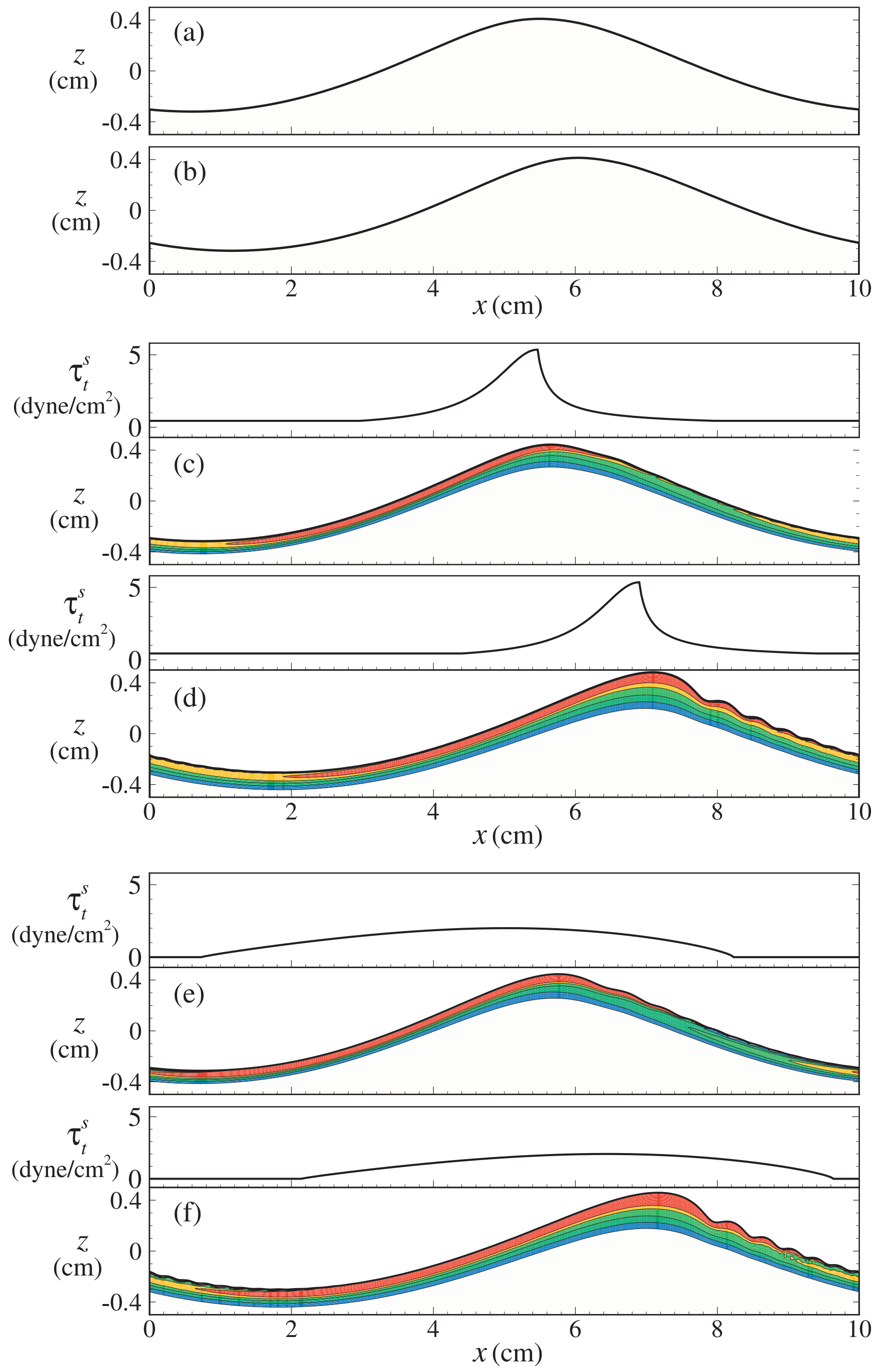

FIG. 24. Instantaneous distributions of the surface profiles and the underlying vorticity fields for the GCW of $\lambda = 10$ cm and $a_0k = 0.23$ subject to three types of tangential-stress boundary conditions at $t =$ (a),(c),(e) $2T_0$ and (b),(d),(f) $4T_0$. (a),(b) The results for the free-propagating GCW with no shear stress at the water surface; (c),(d) the distributions for the same GCW but is driven by the tangential surface stress measured by Okuda (1982); and (e),(f) the distributions for the GCW driven by the shear-stress measurement of Banner and Peirson (1998). The corresponding distributions of the exerting shear stress at the water surface are plotted at top of (c)–(f). Five contours are shown with vorticity values evenly distributed ranging from 20 to 60 s^{-1}. The areas in red are regions with vorticities higher than 60 s^{-1}. The GCW propagates from left to right.

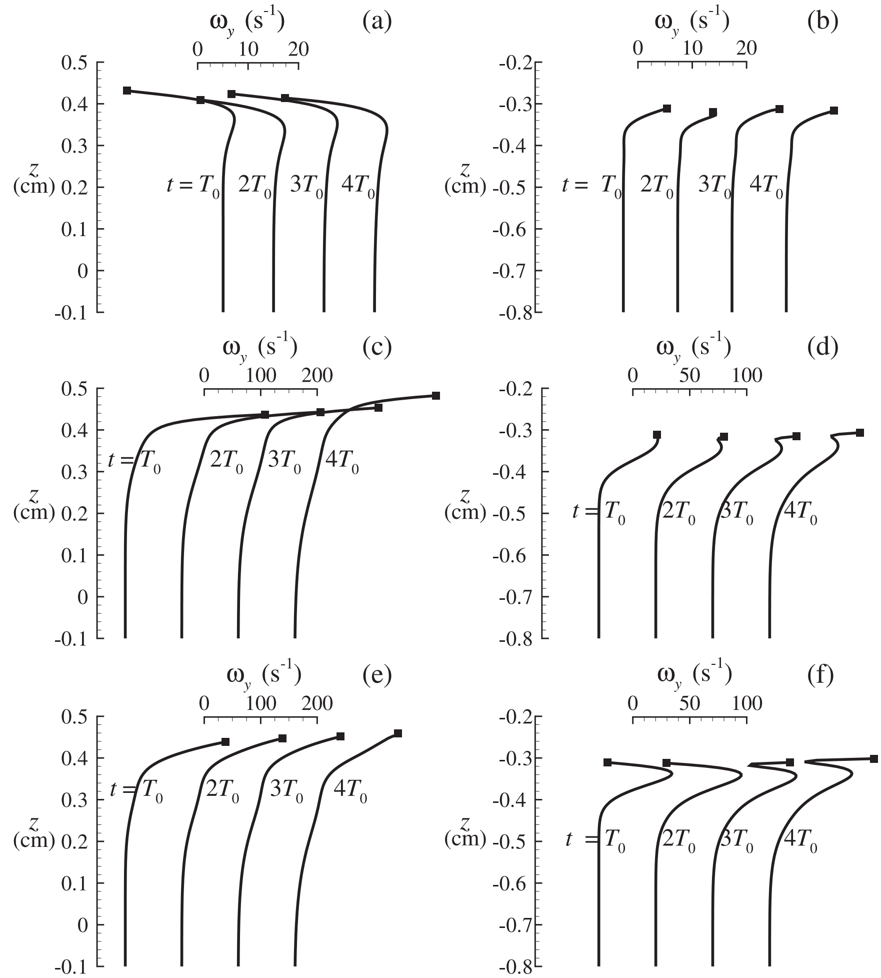

FIG. 25. Vertical distributions of vorticity ω_y (s^{-1}) below the GCW (a),(c),(e) crest and (b),(d),(f) trough for λ = 10 cm and a_0k = 0.23 subject to three types of tangential-stress boundary conditions at times $t = T_0, 2T_0, 3T_0$, and $4T_0$. (a),(b) The results for the free-propagating GCW with no shear stress at the water surface; (c),(d) the distributions for the same GCW but is driven by the tangential surface stress measured by Okuda (1982); and (e),(f) the distributions for the GCW driven by the shear-stress measurement of Banner and Peirson (1998). Note that for clarity the distributions at various times are shifted. The horizontal scale of the vorticity ω_y is the same for the four distributions in each panel, but varies in different panels. Since the flow is irrotational in the submerged water, the vertical distribution of the vorticity quickly attenuate to a vanishing value away from the water surface.

vortex layer underneath the GCW crest indeed is thicker than those beneath the forward and backward surfaces of the GCW. Underneath the GCW trough, a new thin vortical layer immediately next to the water surface is induced by the formation of the capillary ripples (see $t = 3T_0$ and $4T_0$ in Figs. 25d,f). The present numerical experiment therefore demonstrates that the formation of a crest roller within a wind-generated GCW can be attributed to both local wind stress as observed by Okuda (1982) and parasitic capillary ripples as suggested by Longuet-Higgins (1992). Despite the distinct difference in the surface stress distributions, the vorticity fields resemble one another under the two stress-driven water surfaces; and are also similar to the observation of Okuda (1982) in both pattern and strength (see Okuda's Fig. 3).

In this study, we have only considered the formation and evolution of parasitic capillary ripples on two-dimensional GCWs, although our developed numerical model is capable of simulating three-dimensional flows. Parasitic ripples commonly appear with more irregular patterns and exhibit high intermittency on natural water surfaces (e.g., Ebuchi et al. 1987; Zhang 1995). In addition to the capillary trains trapped ahead of the crest, predominant streaks aligned in the wind direction are also observed on the backward face of a wind-driven GCW (Ebuchi et al. 1987). The vortical structures underneath these surface features, therefore, are certainly three dimensional. These vortical layers can also lead to separation and, eventually, the flow becomes turbulent (Qiao and Duncan 2001). To shed light on these more complex flow structures, we are currently conducting full three-dimensional simulations.

Acknowledgments. This work was supported by grants from the National Science Council of Taiwan under Contracts NSC 94-2611-M-008-001 and 95-2611-M-008-006-MY3. The constructive comments of two anonymous reviewers led to an improved presentation of the results. In particular, one reviewer stimulated us to place our numerical results in a wider perspective with respect to other capillary-formation mechanisms related to steady gravity–capillary waves, and also assisted us so that we were better explain the possible origin of recurrent modulation.

REFERENCES

Banner, M. L., and W. L. Peirson, 1998: Tangential stress beneath wind-driven air–water interfaces. *J. Fluid Mech.,* **364,** 115–145.

Chang, J. H., R. N. Wagner, and H. C. Yuen, 1978: Measurement of high frequency capillary waves on steep gravity waves. *J. Fluid Mech.,* **86,** 401–413.

Chen, B., and P. G. Saffman, 1979: Steady gravity-capillary waves on deep water. I. Weakly nonlinear waves. *Stud. Appl. Math.,* **60,** 183–210.

——, and ——, 1980: Steady gravity-capillary waves on deep water. II: Numerical results for finite amplitude. *Stud. Appl. Math.,* **62,** 95–111.

Cox, C. S., 1958: Measurements of slopes of high-frequency wind waves. *J. Mar. Res.,* **213,** 95–109.

Duncan, J. H., V. Philomin, M. Behres, and J. Kimmel, 1994: The formation of spilling breaking water waves. *Phys. Fluids,* **6,** 2558–2560.

Ebuchi, N., H. Kawamura, and Y. Toba, 1987: Fine structure of laboratory wind–wave surfaces studied using optical methods. *Bound.-Layer Meteor.,* **39,** 133–151.

Ermakov, S. A., K. D. Ruvinsky, S. G. Salashin, and G. I. Freidman, 1986: Experimental investigations of the generation of capillary–gravity ripples by strongly nonlinear waves on the surface of a deep fluid. *Izv. Atmos. Oceanic Phys.,* **22,** 835–842.

——, ——, and ——, 1988: Local correlation of the characteristics of ripples on the crest of capillary gravity waves with their curvature. *Izv. Atmos. Oceanic Phys.,* **24,** 561–563.

Fedorov, A. V., and W. K. Melville, 1998: Nonlinear gravity–capillary waves with forcing and dissipation. *J. Fluid Mech.,* **354,** 1–42.

——, ——, and A. Rosenberg, 1998: An experimental and numerical study of parasitic capillary waves. *Phys. Fluids,* **10,** 1315–1323.

Fenton, J. D., 1988: The numerical solution of steady water wave problems. *Comput. Geosci.,* **14,** 356–368.

Gade, M., W. Alpers, S. A. Ermakov, H. Huhnerfuss, and P. A. Lange, 1998: Wind–wave tank measurements of bound and freely propagating short gravity–capillary waves. *J. Geophys. Res.,* **103,** 21 697–21 709.

Gharib, M., and A. Weigand, 1996: Experimental studies of vortex disconnection and connection at a free surface. *J. Fluid Mech.,* **321,** 59–86.

Hogan, S. J., 1980: Some effects of surface tension on steep water waves. Part 2. *J. Fluid Mech.,* **96,** 417–445.

——, 1985: The fourth-order evolution equation for deep-water gravity–capillary waves. *Proc. Roy. Soc. London A,* **402,** 359–372.

Lin, H. J., and M. Perlin, 2001: The velocity and vorticity fields beneath gravity–capillary waves exhibiting parasitic ripples. *Wave Motion,* **33,** 245–257.

Lin, J. C., and D. Rockwell, 1995: Evolution of a quasi-steady breaking wave. *J. Fluid Mech.,* **302,** 29–44.

Longuet-Higgins, M., 1963: The generation of capillary waves by steep gravity waves. *J. Fluid Mech.,* **16,** 138–159.

——, 1992: Capillary rollers and bores. *J. Fluid Mech.,* **240,** 659–679.

——, 1995: Parasitic capillary waves: A direct calculation. *J. Fluid Mech.,* **301,** 79–107.

Mui, R. C. Y., and D. G. Dommermuth, 1995: The vortical structure of parasitic capillary waves. *Trans. ASME: J. Fluids Eng.,* **117,** 355–361.

Okuda, K., 1982: Internal flow structure of short wind waves. Part I. On the internal vorticity structure. *J. Oceanogr. Soc. Japan,* **38,** 28–42.

Peirson, W. L., and M. L. Banner, 2003: Aqueous surface layer flows induced by microscale breaking wind waves. *J. Fluid Mech.,* **475,** 1–38.

Perlin, M., H. Lin, and C.-L. Ting, 1993: On parasitic capillary waves generated by steep gravity waves: An experimental investigation with spatial and temporal measurements. *J. Fluid Mech.,* **255,** 597–620.

Plant, W. J., 1997: A model for microwave Doppler sea return at high incidence angles: Bragg scattering from bound, tilted waves. *J. Geophys. Res.,* **102,** 21 131–21 146.

Qiao, H., and J. H. Duncan, 2001: Gentle spilling breakers: Crest flow-field evolution. *J. Fluid Mech.,* **439,** 57–85.

Rood, E. P., 1995: Vorticity interactions with a free surface. *Fluid Vortices*, S. I. Green, Ed., Kluwer Academic Publishers, 687–730.

Ruvinsky, K. D., F. I. Feldstein, and G. I. Freidman, 1991: Numerical simulations of the quasi-stationary stage of ripple excitation by steep gravity-capillary waves. *J. Fluid Mech.,* **230,** 339–353.

Schwartz, L. W., and J.-M. Vanden-Broeck, 1979: Numerical solution of the exact equations for capillary–gravity waves. *J. Fluid Mech.,* **95,** 119–139.

Tsai, W.-T., and L.-P. Hung, 2007: Three-dimensional modeling of small-scale processes in the upper boundary layer bounded by a dynamic ocean surface. *J. Geophys. Res.,* **112,** C02019, doi:10.1029/2006JC003686.

Watson, K. M., and S. B. Buchsbaum, 1996: Interaction of capillary waves with longer waves. Part 1. *J. Fluid Mech.,* **321,** 87–120.

Wu, J. Z., 1995: A theory of three-dimensional interfacial vorticity dynamics. *Phys. Fluids,* **7,** 2375–2395.

Zhang, X., 1995: Capillary–gravity and capillary waves generated in a wind wave tank: Observations and theories. *J. Fluid Mech.,* **289,** 51–82.